Monthly Notices of the ROYAL ASTRONOMICAL SOCIETY

MNRAS **547,** 1–18 (2026) https://doi.org/10.1093/mnras/stag511
Advance Access publication 2026 March 14

Integral field spectroscopy of collisional ring galaxies – I. Stellar population analysis

M. Chow-Martínez [1,2★] A. Robleto-Orús [1,2] Y.D. Mayya [3] J.P. Torres-Papaqui [4] R.A. Ortega-Minakata [5] D.F. Castro-Hidalgo [6] C.A. Caretta [4] J.J. Trejo-Alonso [7] A. Morales-Vargas [8] R. García-Benito [9] H.E. Jácamo-Delgado [10] and M. Gudiño [11]

[1]*Instituto de Geología y Geofísica Benjamin Linder y Héroes de Bocay (IGG-BLyHB), Universidad Nacional Autónoma de Nicaragua, Managua (UNAN-Managua), C.P. 663, Managua, Nicaragua*
[2]*Centro de Investigación de Astrofísica y Ciencias Espaciales (CIACE), Universidad Nacional Autónoma de Nicaragua, Managua (UNAN-Managua), C.P. 663, Managua, Nicaragua*
[3]*Instituto Nacional de Astrofísica, Óptica y Electrónica, Luis E. Erro, Tonantzintla, 72840 Puebla, Mexico*
[4]*Departamento de Astronomía, Universidad de Guanajuato, Callejón de Jalisco S/N, Col. Valenciana, C.P. 36023, Guanajuato, Gto., Mexico*
[5]*Instituto de Radioastronomía y Astrofísica (IRyA), UNAM, Apartado Postal 72-3, Morelia, 58089 Michoacán, Mexico*
[6]*Departamento de Ciencias Exactas, Centro Universitario de la Costa, Universidad de Guadalajara, Puerto Vallarta, Jalisco C.P. 48280, Mexico*
[7]*Facultad de Ingeniería, Universidad Autónoma de Querétaro, Cerro de las Campanas S/N, 76010, Santiago de Querétaro, Qro., Mexico*
[8]*Centro de Astronomía (CITEVA), Universidad de Antofagasta, Avenida U. de Antofagasta 02800, Antofagasta, Chile*
[9]*Instituto de Astrofísica de Andalucía–CSIC, Glorieta de la Astronomía S/N, E-18008 Granada, Spain*
[10]*Departamento de Física, Área de Ciencias Básicas e Ingeniería, Universidad Nacional Autónoma de Nicaragua, Managua (UNAN-Managua), C.P. 663, Managua, Nicaragua*
[11]*Instituto de Astronomía, Universidad Nacional Autónoma de México, AP 70-264, 04510, Ciudad de México, Mexico*

Accepted 2026 March 12. Received 2026 March 10; in original form 2025 August 12

ABSTRACT

Collisional ring galaxies are produced by the collision of a disc galaxy with a compact galaxy plunging through the disc, forming a ring-shaped expanding density wave, triggering star formation at its wake. The wave expansion is expected to produce negative stellar age gradients in radial profiles of post-collision stellar populations. Integral field spectroscopy combined with stellar population synthesis allows us to spatially resolve the stellar populations, to separate the post-collision and pre-collision components, and to produce the radial profiles. We analyse three candidate galaxies: Arp 143, NGC 2793, and VII Zw 466. Observations were performed with the Calar Alto 3.5 m telescope using the PMAS/PPak spectrophotometer. NGC 2793 presents a positive stellar age gradient, dismissing the collision hypothesis. For Arp 143 and VII Zw 466, we found negative stellar age gradients for the youngest stellar populations, up to the ring radii, consistent with the collision hypothesis. We estimated that the collisions occurred ∼300 and ∼100 Myr (expansion velocities of 33 ± 10 and 108 ± 26 km s^{-1}), respectively, before the density waves reached the observed ring radii. A spatially resolved analysis of the specific star formation history (sSFH) reveals an expected star formation enhancement following the collision. The sSFH also allowed us to identify the most probable intruder galaxy for VII Zw 466. We report new redshifts for its group members. Finally, radial profiles of light contributions from pre-collisional and post-collisional stars show that the density wave dragged old pre-collisional stars along, as predicted by simulations.

Key words: galaxies: interactions – galaxies: star formation – galaxies: structure.

1 INTRODUCTION

Ring galaxies are one of the less common morphological types among peculiar galaxies. They are believed to be produced by an infrequent kind of collision (E. M. Burbidge & G. R. Burbidge 1959; E. Athanassoula & A. Bosma 1985): a compact galaxy plunging almost perpendicular through the equatorial plane of a disc galaxy. In this scenario the ring is formed by star-forming regions induced by the passage of a density wave produced by the collision.

This hypothesis was supported by early N-body simulations (e.g. R. Lynds & A. Toomre 1976; J. C. Theys & E. A. Spiegel 1977; M. Mapelli et al. 2008). Later simulations including stellar and gas dynamics, reproduced different ring morphologies and other associated structures, such as the spokes seen in the famous Cartwheel ring galaxy (L. Hernquist & M. L. Weil 1993; C. Struck-Marcell & J. L. Higdon 1993). R. A. Gerber, S. A. Lamb & D. S. Balsara 1996 simulations considered the formation and propagation of the ring based on a Milky Way-like galaxy to reproduce the features of the Cartwheel. They found an expansion velocity

★ E-mail: marcel.chow@unan.edu.ni

of the ring ∼140 km s^{-1} and rotation speeds in the ring up to 450 km s^{-1}. However, these predicted expansion velocities are much higher compared to the 13–30 km s^{-1} obtained observationally (J. L. Higdon, S. D. Lord & G. Cecil 1996; P. Amram et al. 1998). These velocities give Cartwheel kinematical ages between 150 and 400 Myr.

An observational consequence of star formation in an expanding wave is the formation of a colour gradient in the disc galaxy as a new generation of stars is formed at successively outer parts as the density wave passes through. The youngest and brightest blue stars of this new generation dominate the observed light of the star-forming ring in most bands. As the density wave, and the corresponding star-forming ring, advances farther from the centre, it leaves in its wake stellar remnants of massive stars and low-mass stars that mix with the stellar population of the pre-collisional disc. As a result, a colour gradient should be observed with bluer colours (proxy of younger stellar ages) at the position of the ring, and redder colours (proxy of older stellar ages) closer to the impact centre. Most of the observational attempts to test this scenario have focused on the Cartwheel galaxy, given its proximity and relatively large angular size (P. M. Marcum, P. N. Appleton & J. L. Higdon 1992; V. Korchagin, Y. D. Mayya & E. Vorobyov 2001; E. I. Vorobyov & D. Bizyaev 2001).

As for other ring galaxies, the compilation by R. Romano, Y. D. Mayya & E. I. Vorobyov (2008) is the only systematic study to date testing the collision hypothesis for a set of ring galaxy candidates, taken from the P. N. Appleton & C. Struck-Marcell (1987) sample. R. Romano et al. (2008) measured the Hα intensity and colour radial profiles for fifteen ring galaxy candidates, showing that at least nine of them present radial colour gradients consistent with the propagation of the star formation wave. However they found that the observed colour gradient has an important contribution from the intrinsic colour gradient existing in the discs of galaxies.

The last decade has seen drastic advances in both computational and observational fronts that are impacting all fields of astronomy. The most notable advancement in the simulation of ring galaxies is the one by F. Renaud et al. (2018), who carried out hydrodynamical simulations of Cartwheel-kind of interactions using an adaptive mesh refinement code to couple the galactic scale dynamics with star formation reaching spatial scales of 6 pc. According to these more realistic simulations, the newly formed stars are dragged by the wave before falling back into the central regions at later stages. In this expanding material wave scenario, a wide range of ages are expected in the ring regions.

J. Zaragoza-Cardiel et al. (2022) carried out such a study of the Cartwheel galaxy using the Multi Unit Spectroscopic Explorer (MUSE) data. They found that the radial gradient of the present-day gas-phase metallicities supports the predictions of F. Renaud et al. (2018) scenario of an expanding material wave. More recently, F. R. Ditrani et al. (2024) derived star formation history (SFH) from the same MUSE data. They concluded that the observed spectral flux of the ring is dominated mostly by the youngest, luminous post-collisional stars. On the other hand, Y. D. Mayya et al. 2024, using the UV images of the Cartwheel galaxy, reported that the star-forming ring consists of stellar populations formed over the last 150 Myr. They also found evidence for the presence of an age gradient of the populations formed in the wake of the expanding wave as predicted by the classical density wave models. These observations suggest that the correct picture is somewhere in between with some of the stars formed by the expanding wave remaining at the location of their formation while some stars are dragged by the wave.

The most notable advance on the observational front is the integral field spectroscopy (IFS, e.g. P. T. Zeeuw et al. 2002; S. F. Sánchez et al. 2012; K. Bundy et al. 2015), which allows spatially resolved analysis of the spectra over the entire galaxy using stellar population synthesis models (e.g. C. Conroy 2013; A. Vazdekis et al. 2016; C. Maraston et al. 2020) to disentangle the current star formation rate (e.g. C. Catalán-Torrecilla et al. 2015, 2017; S. L. Ellison et al. 2018; A. Morales-Vargas et al. 2020) as well as the complete SFH (e.g. H. J. Ibarra-Medel et al. 2016; O. López-Cruz et al. 2019; F. R. Ditrani et al. 2024). This technique allows us to study the spatial distribution of the stellar populations and their properties such as their age, metallicity, and kinematics. In this work, we present IFS observations of three ring galaxies – selected from the R. Romano et al. (2008) sample – in order to test the collision hypothesis by searching for age gradients: Arp 143, NGC 2793 and VII Zw 466. While R. Romano et al. (2008) used colour gradients as proxies for stellar age gradients, the IFS observations combined with stellar population synthesis models allow us to infer the presence of stellar populations in the discs from both the post and pre-collisional star formation through the detection of their characteristic spectral features. We found that both Arp 143 and VII Zw 466 are consistent with what is expected for collisional ring galaxies, while NGC 2793 appears to be an ordinary dwarf galaxy. In order to explain how we got to this conclusion, we show here the analysis of these three galaxies.

The paper is organized as follows: the observations and the reduction process are presented in Section 2. Section 3 shows the methodology and analysis of the data. The results are described in Section 4. Finally, Section 5 discusses the conclusions. Throughout the paper, a standard cosmology, with a Hubble–Lemaitre constant of $H_0 = 70$ km s^{-1}, $\Omega_\Lambda = 0.7$ and $\Omega_M = 0.3$ is assumed.

2 OBSERVATIONS AND DATA REDUCTION

The observations were carried out with the 3.5 m telescope at the Calar Alto Observatory (Almería, Spain), using the PMAS/PPak spectrophotometer, across two nights (2016 March 28th and 30th). We observed eight galaxies from the R. Romano et al. (2008) sample. Three of them are presented in this paper (see Table 1).

During the observations, there were acceptable weather conditions with a mean seeing full width at half-maximum (FWHM) of 1.5 arcsec. We used the V500 (R∼850) and V1200 (R∼1650) gratings for the three objects, with integration times of 900 and 1800 s, respectively, with three exposures per field per grating. This allowed us to adopt the three-pointing dithering scheme used by the CALIFA survey (The Calar Alto Legacy Integral Field Area Survey, S. F. Sánchez et al. 2012). This scheme reaches a 100 per cent filling factor across the entire field of view by combining three slightly offset pointings of the telescope, compensating for the spaces between the instrument optical fibres. In addition, sky flats and spectra of standard stars were acquired for the reduction process.

The reduction was performed using the pipeline described in B. Husemann et al. (2013), R. García-Benito et al. (2015) and S. F. Sánchez et al. (2016), following the CALIFA reduction scheme: the raw observation pass through a semi-automatic reduction, including bias subtraction, cosmic rays removal, arc lamp calibration, wavelength solution and flux calibration.

The three dithering exposures of each field for each grating were combined into a single data cube. Then, the V1200 data cubes were spectrally combined with the V500 into a combined (COMB) data cube by averaging the flux in the overlapping wave-

Table 1. General description of the sample of observed galaxies. For VII Zw 466 we observed two offset but overlapped fields to analyse the companion galaxies in the group, searching for the possible colliding companion. Coordinates and B_r magnitudes (in Vega system) are taken from the P. N. Appleton & C. Struck-Marcell (1987) catalogue. These coordinates are close to but not exactly at the centre of the image, nor at the centre of the galaxy. Ring radii were taken from R. Romano et al. (2008) and correspond to semimajor axes derived from ellipses fitted to Hα emission.

Galaxy	RA (h m s)	Dec. (° ′ ″)	Redshift	Redshift Reference	Distance (Mpc)	B_r (mag)	Ring radius (″)	Exp. Time (h)	Mean Airmass
Arp 143	07 46 52	+ 39 00 36	0.01295	L. Galbany et al. 2018	59	13.6	36	2.25	1.04
NGC 2793	09 16 47	+ 34 25 47	0.00563	C. M. Springob et al. 2005	28	14.2	20	2.25	1.05
VII Zw 466	12 31 56	+ 66 24 41	0.04833	J. Corwin, R. J. Buta & G. de Vaucouleurs 1994	215	14.6	11	4.50	1.15

length region and resampling the V1200 spectral range to V500 resolution. This strategy compensates for internal vignetting in the blue range (3745–4240 Å) of the V500 grating (see S. F. Sánchez et al. 2012 for details). The resulting spectral sampling is 2.0, 0.7, and 2.0 Å for the V500, V1200, and COMB data cubes, respectively. For this work, we used only the resulting COMB data cubes with a combined spectral range from 3745 to 7501 Å. The nominal resolution of these combined spectra is FWHM $\sim$ 6.5 Å, actually the same as V500.

3 ANALYSIS METHODS

3.1 Stellar population synthesis

We performed the stellar population synthesis using the STARLIGHT code (R. Cid Fernandes et al. 2005). STARLIGHT fits each spectrum to a combination of simple stellar populations (SSPs), by estimating the percentage of each SSP contributes to the spectrum starlight flux, to the 'present-day' stellar mass, and to the initial stellar mass.

We used a selection of SSPs based on the work of A. Mateus et al. (2006), comprising 150 SSPs covering 25 ages (logarithmically spaced from 1 Myr to 18 Gyr) and 6 metallicities: Z= 0.005, 0.02, 0.2, 0.4, 1.0, and 2.5 $Z_\odot$. The chosen age and metallicity ranges include values expected for both pre- and post-collision star formation events. These SSPs correspond to the 2016 version of the G. Bruzual & S. Charlot (2003) stellar population models[1], at a resolution with an FWHM of 2.3 Å. While we follow the general approach of A. Mateus et al. (2006), we introduce a modification by adopting the MILES stellar library (P. Sánchez-Blázquez et al. 2006; A. Vazdekis et al. 2010; J. Falcón-Barroso et al. 2011). We retain the original Padova stellar evolutionary tracks (G. Bertelli et al. 1994) and the G. Chabrier (2003) Initial Mass Function (IMF), and apply the reddening law of J. A. Cardelli, G. C. Clayton & J. S. Mathis (1989) with $R_V = 3.1$. This recipe has satisfactorily been used by A. Morales-Vargas et al. (2020) for PMAS/PPak data.

The spectra extracted from the COMB data cubes were prepared for the STARLIGHT fitting process by shifting the spectra to the galaxy rest frame, resampling to a wavelength interval of $\Delta\lambda = 1.0$ Å and masking out the emission lines, following the STARLIGHT manual[2] Errors were propagated using a covariance matrix accounting for both the fraction of flux within each new $\Delta\lambda$ interval and the quadrature sum of the uncertainties from the original spectra (see A. C. Carnall 2017 for details).

STARLIGHT then uses a Markov chain Monte Carlo (MCMC) method to fit a linear combination of the SSPs to the observed spectrum. The resulting fitted continuum is convolved by a Gaussian kernel whose FWHM is determined by the MCMC. That FWHM is similar (but not exactly equal) to the instrumental FWHM of the observed spectrum combined in quadrature with the FWHM of the SSP spectra used for the linear combination.

The fitting was restricted to the spectral range from 3800 to 7200 Å in order to avoid edge effects. The correction for galactic extinction was applied by using the dust maps produced by D. J. Schlegel, D. P. Finkbeiner & M. Davis 1998. We only accepted STARLIGHT solutions for spaxels with a signal-to-noise ratio (S/N) >10 in the stellar continuum, computed in the window from 5075 to 5125 Å. Representative examples of the spectral fits are presented in Fig. 1.

We calculated the light-weighted mean age[3] $\langle \log t_\star \rangle_L$ and mass-weighted mean age $\langle \log t_\star \rangle_M$, as defined by N. V. Asari et al. (2007):

$$\langle \log t_\star \rangle_L = \sum_{j=1}^{N_\star} x_j \log_{10} t_{\star,j} \quad (1)$$

and

$$\langle \log t_\star \rangle_M = \sum_{j=1}^{N_\star} \mu_j \log_{10} t_{\star,j}, \quad (2)$$

where x_j and μ_j are the starlight flux fraction and stellar mass fraction corresponding to the j-th SSP, respectively, while $t_{\star,j}$ is the age of the j-th SSP and $N_\star$ is the total number of SSPs. Equations (1) and (2) tend to highlight different stellar populations: the light-weighted mean ages tend to yield younger populations, as short-lived massive stars (O, B, and A types) dominate the optical flux when present, despite being less numerous than low-mass stars.

On the other hand, the mass-weighted mean ages tend to yield long-lived low-mass stars (such as G, K, and M stars), because of their large mass-to-light ratio as well as because of their typically large numbers in giant galaxies. The core of these tends is in the statistical nature of the definitions of $\langle \log t_\star \rangle_L$ and $\langle \log t_\star \rangle_M$. For a deeper discussion on this topic, see R. C. Cid Fernandes, J. R. S. Leão & R. R. Lacerda (2003) and R. Cid Fernandes et al. (2004).

STARLIGHT estimates several properties of the stellar populations as output for each spectrum, including mass, stellar extinction, velocity shift and velocity dispersion. The STARLIGHT solution also produces a synthetic spectrum for

[1] http://www.bruzual.org/bc03/Updated_version_2016/
[2] Available at http://www.starlight.ufsc.br/
[3] Weighted by the light contribution of the j-th population to the wavelength range of the spectrum.

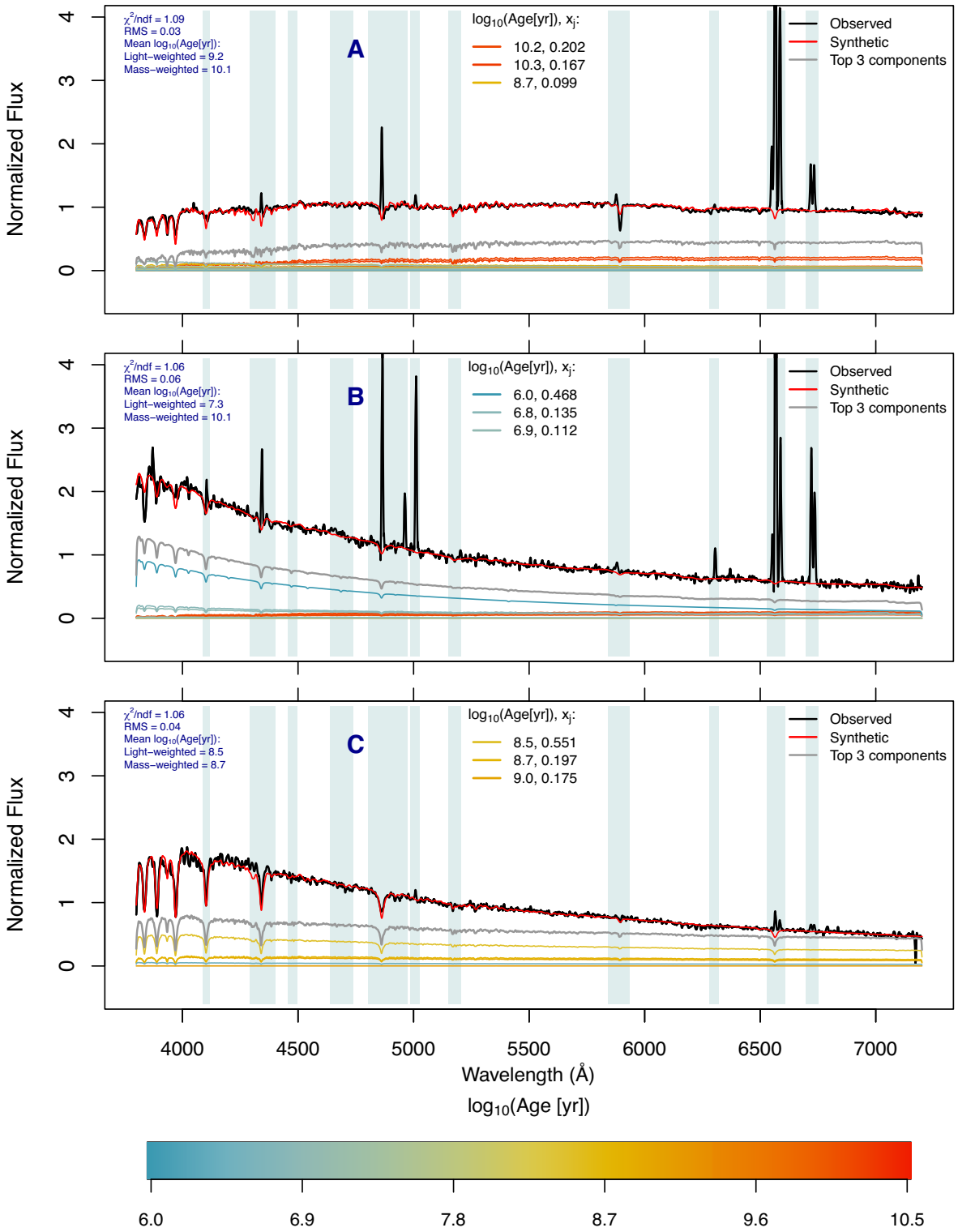

Figure 1. Representative spectral fits for three spaxels in Arp 143. The locations of these spaxels, labelled as A, B, and C, are indicated in Fig. 2, top-left panel. The flux of each spectrum is normalized at $\lambda = 5100$ Å. The observed spectrum is plotted with a solid-black line and the synthetic spectrum with the best-fitting solution is plotted with a red-dashed line. The individual SSP spectra contributing to the solution are plotted as solid coloured lines. Each of these lines represents an SSP spectrum of a given age, integrated over the six metallicities, and scaled by its corresponding population vector component, x_j. The colour of each line corresponds to the age of that stellar population, as indicated by the colour bar at the bottom. In each panel, the central inset legend lists the ages of the three SSPs that most significantly contribute to the synthetic spectrum (the top three components). The solid grey line represents the sum of these three SSPs. The shaded regions indicate the spectral intervals that were masked out during the STARLIGHT fit to exclude emission lines. The goodness-of-fit parameters, χ^2/ndf and the RMS, are shown in the top-left corner, along with the light-weighted and mass-weighted mean stellar ages for each spaxel, computed using equations (1) and (2).

the stellar continuum, which is the sum of the flux contribution of all the SSPs to each wavelength (including dust extinction), being a good approximation to the observed stellar continuum without the emission features.

3.2 Emission line analysis

The fitted synthetic stellar continuum from each spaxel was subtracted from the observed spectrum to obtain a 'pure emission' spectrum. We fitted single-Gaussian models to the profiles of the different emission lines, using a Levenberg–Marquardt algorithm (K. Levenberg 1944; D. W. Marquardt 1963) and the LAPACK Fortran libraries (E. Anderson et al. 1999). Extinction correction of the emission line fluxes was performed using the Balmer flux ratio $F_{H\alpha}/F_{H\beta} = 2.86$ for case B recombination (M. Brocklehurst 1971), using the J. A. Cardelli et al. (1989) extinction law.

In this first paper, we used the H α emission as a tracer for star formation. The detailed analysis of the ionized gas properties using other emission lines will be presented in a future paper (Robleto-Orús et al., in preparation). We applied a threshold of S/N > 3 to the H α emission line in all spaxels.

4 RESULTS

Fig. 2 (left panels) shows synthetic RGB images of the three galaxies, produced by combining the extracted fluxes of the Johnson–Cousins *BVR* bands from the data cubes. The H α luminosity is a good tracer for the ring position in this kind of galaxy, as shown by R. Romano et al. (2008). We plotted the H α emission contours in all maps for brightness at 0.1 $L_{\odot}$ kpc^{-2} obtained from spaxels with S/N > 3 for the line flux.

Light-weighted age $\langle \log t_{\star} \rangle_L$ and mass-weighted age $\langle \log t_{\star} \rangle_M$ maps of the three galaxies are shown in the centre and right columns of Fig. 2, respectively. For all galaxies, the location of the youngest populations in the light-weighted maps is consistent with the H α contours, serving as a sanity check of the procedure followed in this work. On the other hand, the mass-weighted ages are almost uniform across the disc, with these ages systematically larger than the light-weighted ages. As a result, and as it was mentioned in Section 3.1, the light-weighted maps show younger mean ages than mass-weighted maps.

The difference between the light-weighted and mass-weighted ages is easily discernible in Fig. 3, which shows box plots of the distribution of the light-weighted and mass-weighted ages for the spaxels of each galaxy. In the three cases, the median of the total distribution of light-weighted ages ($\sim 10^8$ yr) is almost two orders of magnitude lower than the mass-weighted age ($\sim 10^{10}$ yr).

In the context of the collisional scenario of ring formation, the light-weighted ages correspond to those of the populations that formed after the collision, whereas the mass-weighted ages correspond to those of the pre-collisional disc populations. In the rest of this section, we carry out a detailed analysis of the relative distribution of these two populations as a function of the distance from the ring centre.

4.1 Age profiles

In order to produce age profiles we need to consider projection effects in the plane of the sky. R. Romano et al. (2008) accounted for these by fitting ellipses in both *B*-band (Johnson–Cousins) and H α images. The first is more consistent with the stellar disc, whereas the second better traces the ring. The parameters of these ellipses (centres, semi-major axes, ellipticities and position angles) are listed in table 4 by R. Romano et al. (2008). In this work we use their H α image parameters to de-project the radial distances of the spaxels with respect to the ring, since their images have better spatial resolution than our IFS data.

In the density wave scenario of ring formation (R. Lynds & A. Toomre 1976), the wave expands around the impact point resulting in an expanding star formation wave. The star formation is quenched in the wake of the expanding wave due to the consumption of gas and the negative feedback from dying stars resulting in the youngest stars located at the ring position and successively older stellar populations towards the inner regions. In the more recent ring simulations by F. Renaud et al. (2018) some of the formed stars are dragged by the expanding wave, resulting in the appearance of post-collisional stars of all ages, not just the youngest, at the ring position. In order to test these models, we need to ideally construct age profiles radially symmetric around the impact point. However, since locating the impact point in ring galaxies is a non-trivial exercise, in this analysis we consider the centre of the ellipses as the impact point. The possibility of off-centre collisions and the nature of the ring they produce will be discussed in Section 5.

We used the R. Romano et al. (2008) H α ellipse parameters to calculate the de-projected radial distances of the spaxels. Fig. 4 shows the mean light-weighted age versus de-projected radial distance profiles for each spaxel in the three galaxies within the radial distance of 1.2 times the semi-major axis of the ring. The position of the ring from R. Romano et al. (2008) is shown by the vertical blue dashed line. For each galaxy, the plot shows the median age of all spaxels (in green) and a least-squares fit (in red). Stellar populations cover a large range of ages at each radial distance. Under the collision interpretation for ring galaxies, the upper boundary corresponds to the pre-collisional old disc stars and the lower boundary denotes the age of the last episode of star formation at that radius. To probe if this is the case, we need to analyse the radial gradient of the youngest populations (the ones assumed to be created during the collision, which is presented in Section 4.2).

In order to illustrate better the radial and azimuthal distributions of median ages of the stellar populations from the impact point up to the ring, we use box plots in Fig. 5, selecting the spaxels in bins of 3.0 arcsec (twice the FWHM of the seeing). We restricted the analysis of the azimuthal distributions to four quadrants. The quadrants follow the Cartesian quadrants with the centres fixed to the centre of the R. Romano et al. (2008) H α ellipses, which is the assumed impact point. The top-most panel for each galaxy shows the profile for the whole galaxy, which is henceforth referred to as the 'general profile', with the bottom four panels showing it for the quadrant indicated in the bottom-left inset in each panel.

4.2 Profiles of the youngest populations

Fig. 5 shows that even for $\langle \log t_{\star} \rangle_L$ – which should be biased towards young ages – many spaxels close to the centre of the ring, the assumed impact point, show median ages well above 10^8 yr, the ring lifetime expected from the models of Cartwheel-like ring galaxies (F. Renaud et al. 2018). This is most likely due to a mix of the old populations present in the galaxy before the collision with the new populations created by the passage of the ring density wave. R. Romano et al. (2008) arrived at similar conclusions in the case of the colour gradients. As the density wave generated after the ring-making impact expands, it forms stars at the position

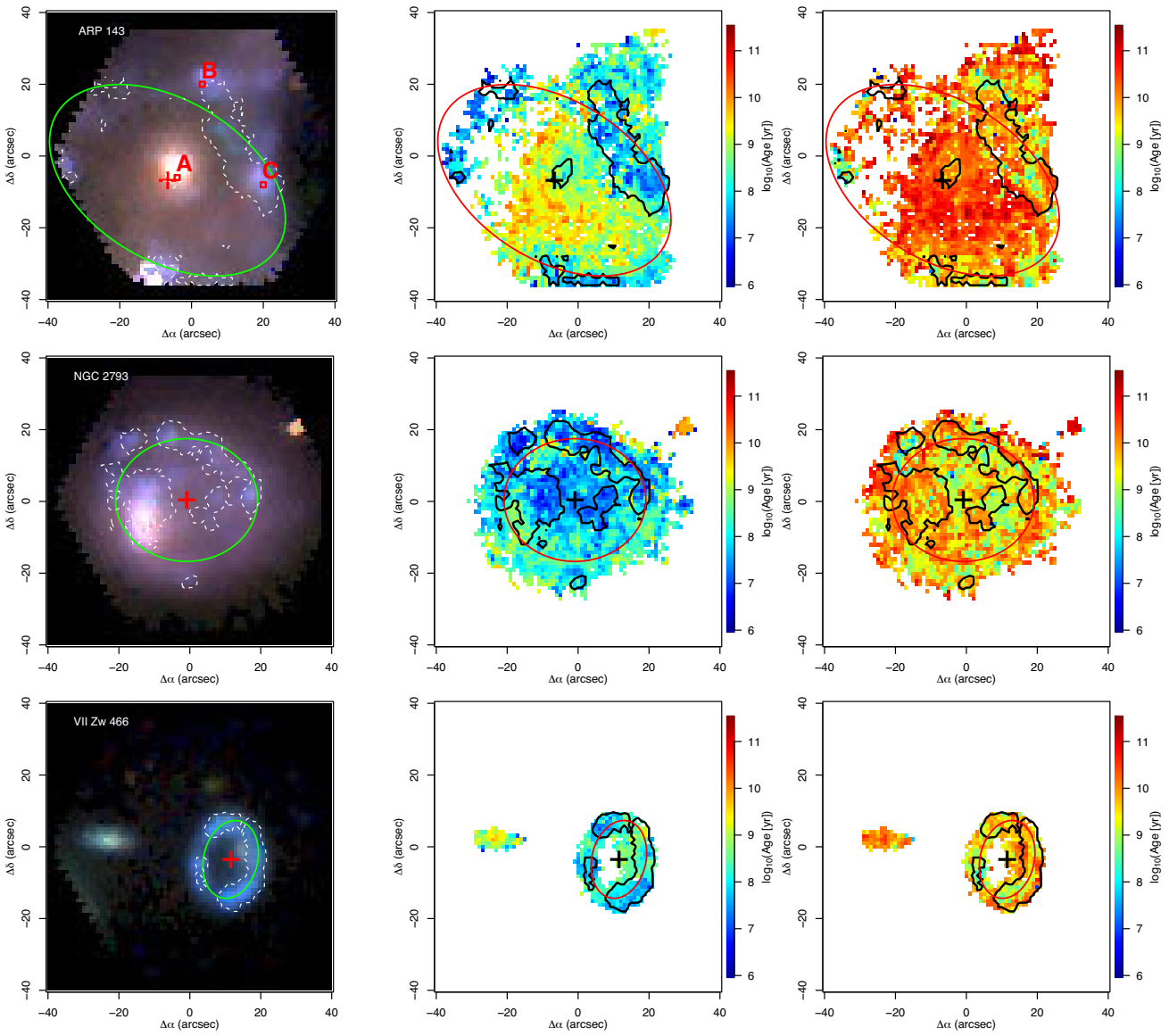

Figure 2. Left panels: RGB images of the observed galaxies produced by extracting the BVR Johnson synthetic bands from the IFS data cubes. Central panels: light-weighted mean age maps ($\langle \log t_\star \rangle_L$). Right panels: mass-weighted mean age maps ($\langle \log t_\star \rangle_M$). Contours in all maps represent Hα surface brightness at 0.1 $L_\odot$ kpc^{-2} obtained from spaxels with S/N $>$ 3 for Hα. Ellipses were taken from the R. Romano et al. (2008) fit over the Hα band, with the crosses marking the centres of those ellipses. The relative coordinates of these maps are in relation to the IFS image centre (see coordinates in Table 1). North is up and East is to the left. For Arp 143 (top-left panel), the labels A, B, and C correspond to the position of the spaxels presented in Fig. 1.

of the wave. The star formation is eventually quenched in the wake of the wave due to negative feedback from the exploding supernovae, as well as due to gas consumption (V. Korchagin et al. 2001). Under such a scenario, the age of the youngest population at any given radius could be approximated as the epoch when the ring passed that radius, with the youngest age at the impact point corresponding to the epoch of impact. Such a scenario predicts a negative radial age gradient of the youngest populations.

We take advantage of the box plot profiles to isolate the spaxels dominated by the youngest populations at each radius. For this we considered only those spaxels with ages contained within the lower whisker and the first quartile (Q1) in Fig. 5. By convention, the lower whisker of a box plot begins at Q1 (top) and ends at the lowest observed data point of the distribution that is still 1.5 times the inter-quartile range [IQR $= Q3 - Q1$, the range within the first and third quartiles (Q1 and Q3)] from Q1 (bottom). All data points outside the whisker boundaries are considered as outliers. This is a pure statistical definition that accounts only for the distribution in each bin of the box plots in Fig. 5. The youngest populations defined in this way in each quadrant of the three sample galaxies are shown in Fig. 6. A comparison of the ages of the youngest population at the normalized radius in the three galaxies is carried out in Fig. 7.

Once we have the profiles, we define the gradient of the mean age of the youngest populations (as defined above) as

$$\nabla t_{\star y} = \frac{\langle \log t_\star \rangle_y^{R=R_{\rm ring}} - \langle \log t_\star \rangle_y^{R=0.5R_{\rm ring}}}{0.5\ R_{\rm ring}}, \quad (3)$$

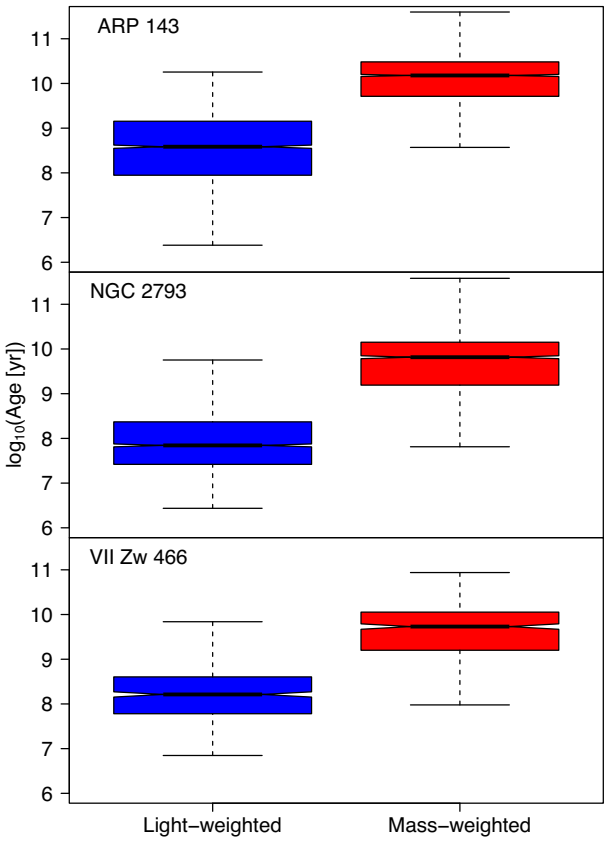

Figure 3. Box plots of the distribution of light-weighted ($\langle \log t_\star \rangle_L$) and mass-weighted ($\langle \log t_\star \rangle_M$) ages for the three galaxies of our sample. As for any classical box plot, the box contains data points between the first and third quartiles, and the whiskers represent the distance to the farthest data points within 1.5 times the interquartile range (IQR). Bold lines mark the median, while the notches represent the confidence interval around that median. The S/N > 10 criterion was applied beforehand. For VII Zw 466, only spaxels on the ring galaxy were included.

where $\langle \log t_\star \rangle_y^{R=R_{\rm ring}}$ and $\langle \log t_\star \rangle_y^{R=0.5R_{\rm ring}}$ are the mean ages of the 'youngest' populations, for the bin at the ring location and for half the ring radius, respectively. Both values were obtained by interpolating the ages of the spaxels contained by the two bins closest to such locations. We computed the mean gradient directly instead of deriving it from linear regression because we are analysing not a dispersed set of points but the extreme values of the lower whisker in box plots. Calculating the difference between two well-separated points provides a more robust estimate, as intermediate points could be influenced by internal trends within the profiles.

The choice of determining the gradient between $R = 0.5R_{\rm ring}$ and $R_{\rm ring}$ rather than the entire extent of the ring is based on the following three reasons: (1) the difficulty in isolating the youngest population close to the central regions as they are affected by older populations by a greater extent as compared to outer regions, (2) the central regions have lesser number of spaxels for a statistically significant analysis, and (3) the assumption of the ellipse centre as the impact point makes a lesser effect at outer radii, especially in small angular sized galaxies such as VII Zw 466. The quantity $\nabla t_{\star y}$ has units of $\log_{10}$(Age[yr]), and coincides with the gradient if we use the normalized radius at $R_{\rm ring}$.

Table 2 lists the values of $\nabla t_{\star y}$ for the whole galaxy profiles and for the four quadrants for each galaxy. In the case of VII Zw 466, as mentioned previously, only western quadrants were used to compute $\nabla t_{\star y}$, despite the values of each quadrant were indicated in the table. In general, Arp 143 and VII Zw 466 show the most significant gradients, both with $\nabla t_{\star y} \leq -1.0$, while NGC 2793 is consistent with a flatter gradient.

We use the plots in Figs 3–7 to discuss the three galaxies under the collisional scenario of ring formation following the classical models of J. C. Theys & E. A. Spiegel (1976) and the more recent simulation of F. Renaud et al. (2018) in the next subsection.

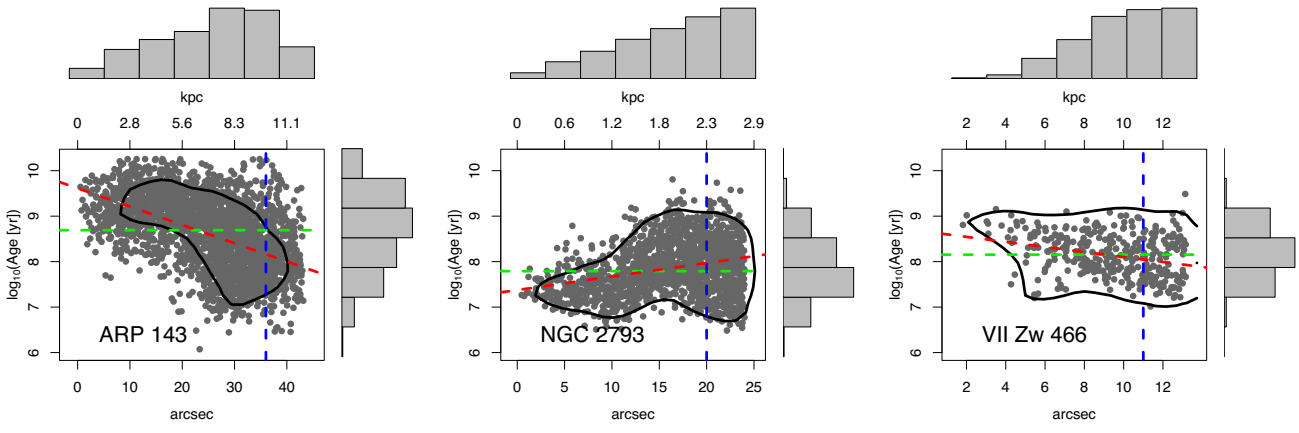

Figure 4. De-projected radius versus mean age (light-weighted) radial profiles for each galaxy. The radii of the spaxels were de-projected using the H α ellipse parameters of R. Romano et al. 2008. The black contours represent the 90 per cent probability of finding a point. The green dashed lines represent the median age of the spaxel distributions. The red dashed lines represent the least-squares fit to the points. Blue vertical lines mark the semi-major axis distance (ring position). Histograms of the radial and age distribution of the spaxels are shown along box borders. Only spaxels within 1.2 times the semi-major axis distances were considered.

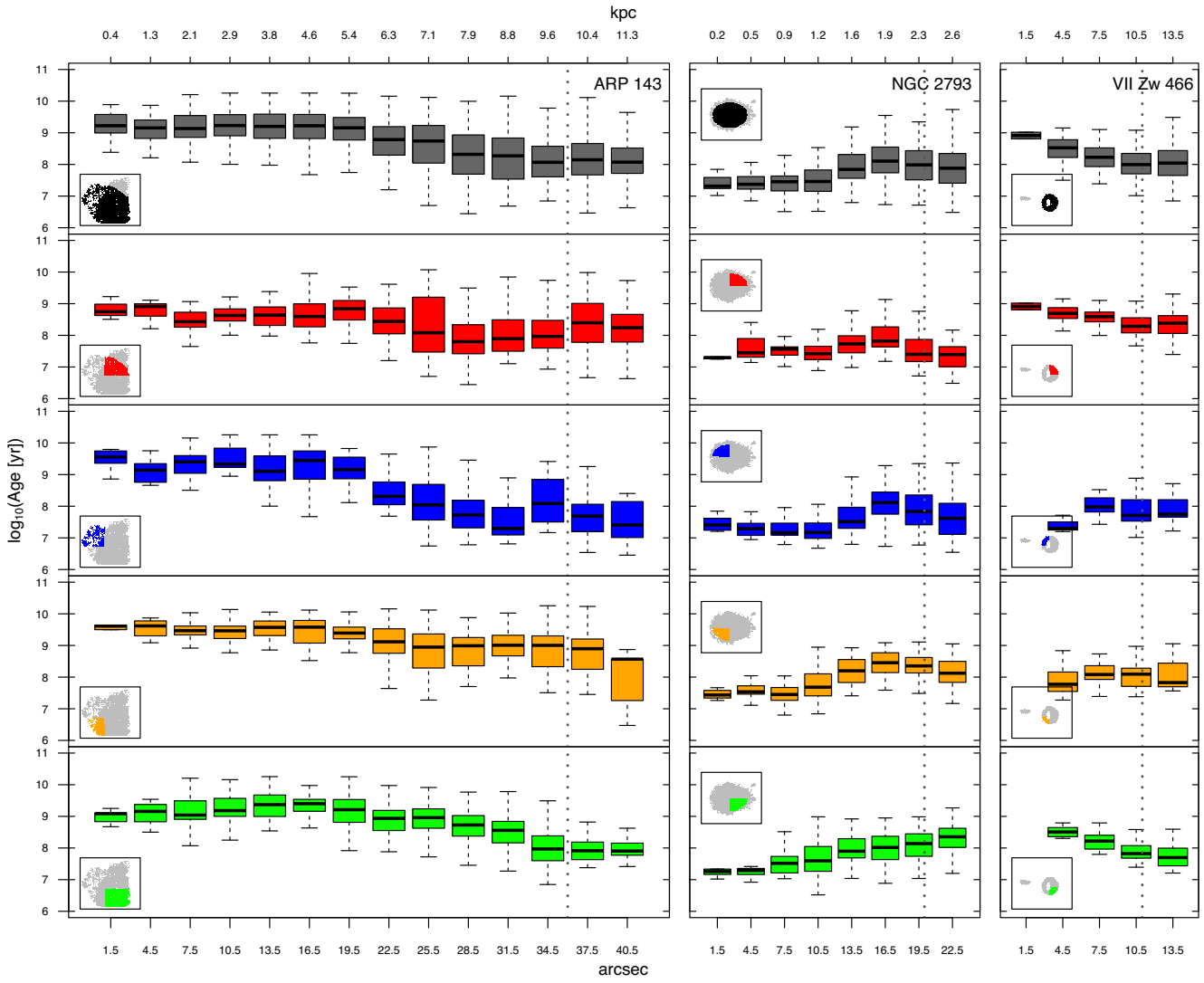

Figure 5. Box plot profiles for the light-weighted age distribution for the three galaxies. The inset maps highlight the spaxels used to produce the profiles. The top panel includes the general profile (i.e. the four quadrants of the disc together) while each of the other panels corresponds to each of the quadrants. The galactocentric radii are measured with respect to the centre of the R. Romano et al. (2008) H α ellipses and the distances are de-projected from the plane of the sky. The bins have a width of 3.0 arcsec (i.e. twice the FWHM of the seeing). Box plots are drawn only if the number of spaxels in the bin is higher than five. The maximum bin extends to 1.2 times the semimajor axis, as indicated by the vertical dotted line. Box plots are defined as in Fig. 3.

4.3 Ages of post-collisional stellar populations in the sample galaxies

4.3.1 Arp 143

Arp 143 exhibits a ring formed by knots of star formation and disrupted material (see Fig. 2). Notably, the B-band emission previously reported by R. Romano et al. (2008) as a tracer for stars in the disc, reaches larger galactocentric distances than the H α emission. This B-band emission extends beyond our field of view. Nevertheless, the star formation ring traced by the H α emission is mostly contained within our field of view except for parts of the north-east quadrant, marked by the green ellipse in Fig. 2. The companion is located to the north-west (outside of the observed field) and the original bulge of Arp 143 is located in the inner region, although presenting a slight offset towards the companion with respect to the centre of the ring.

Consistent with R. Romano et al. (2008) and J. L. Higdon, R. J. Rand & S. D. Lord (1997), we also detected H α emission from the nucleus, pointing to the existence of star formation in that region. J. L. Higdon et al. (1997) suggested that the collision could have produced a long H I tidal tail that funnels gas towards the centre of Arp 143, which could be fuelling the star formation. The fact that the apparent bulge has an offset with respect to the centre of the ring is consistent with an off-centred collision scenario, resulting in important asymmetries in the age maps (see Fig. 2).

The box plot profiles present negative gradients for all quadrants, with the north-west quadrant (red) being the one with the flattest gradient and the north-east quadrant (blue) being the steepest. The lower boundary of points for Arp 143 (Fig. 4) presents a much steeper negative age gradient as compared to the median ages, with the populations being the youngest at the position of the ring, as expected for ring galaxies. A systematic ageing of the population towards the centre of the ring is easily notice-

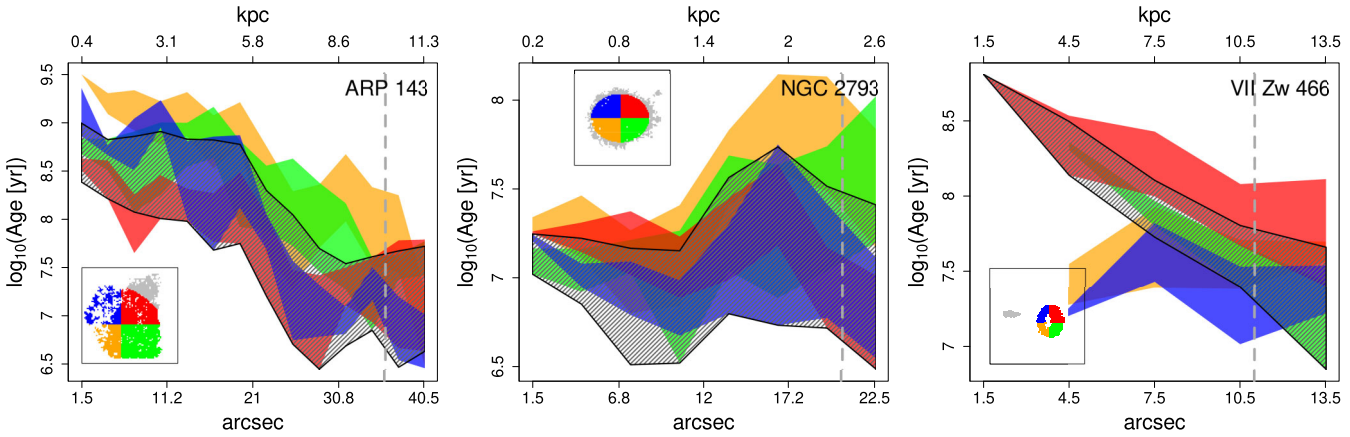

Figure 6. Profiles for the radial distribution of the youngest spaxels, i.e. any spaxel between the lower whisker and the quartile Q1 of the box plots of Fig. 5. Colours indicate the profile in the direction of the corresponding quadrant indicated in the inset of each panel. The general profile is marked with hatched black. Grey dashed lines indicate the semi-major axis radius of the rings. We include the (de-projected) physical radius at the upper axis and the observed angular radius at the lower axis. For VII Zw 466, the general profile only includes the western quadrants.

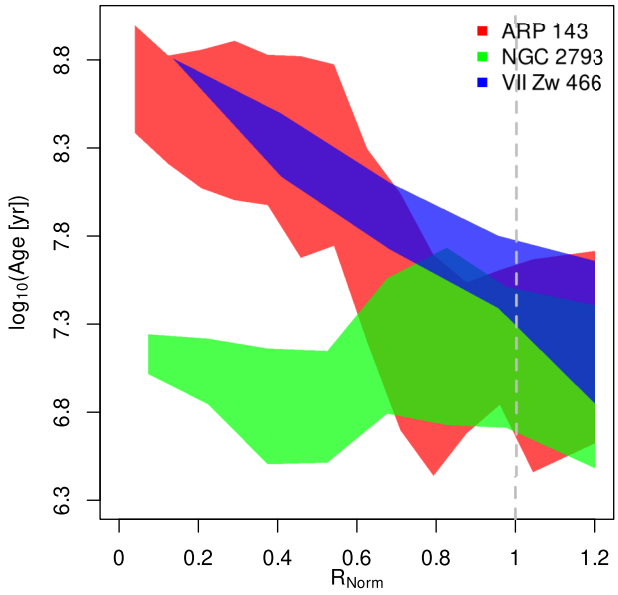

Figure 7. Comparison of the youngest population age profiles for the three galaxies, with their radii normalized at the ring position (R_{Norm}).

able in radial profiles for all the four quadrants. The youngest ages for the four quadrants at the same radius span almost an order of magnitude spread with the ages in the north-western quadrant (red) being systematically younger. The systematic difference of ages in the four quadrants at a given radius suggests different amounts of contamination from pre-collisional disc populations in different quadrants. We take the profile of the quadrant with the youngest ages to determine the minimum age elapsed since the collision. This age corresponds to 300 Myr at the ring centre, reaching 100 and 50 Myr at 25 per cent and 50 per cent ring radius.

4.3.2 NGC 2793

With a mass of 4×10^9 $M_\odot$ (R. Romano et al. 2008), NGC 2793 is the lowest mass ring galaxy candidate of our sample. The physical size of the ring in NGC 2793 is only 2.1 kpc, in spite of its relatively large angular size of 22.5 arcsec (the second largest of our sample). The physical size of the galaxy (4.2 kpc) is also small and is typical of a dwarf galaxy.

The inner regions of NGC 2793 are characterized by young and intermediate age populations (Fig. 2). This is consistent with R. Romano et al. (2008), who found NGC 2793 to be the galaxy with the highest B-band intensity of their sample in the inner regions (>0.2 mag at the centre). The supposed ring-structure is clearly traced by the Hα emission except for the south-west quadrant, where it is almost absent. The age profile of NGC 2793 (Fig. 4, centre) presents a positive gradient inconsistent with the collision hypothesis.

The age profile in NGC 2793 is dominated by spaxels with ages of $10^{7-7.3}$ yr at the first bin (1.5 arcsec) in Fig. 5 (top panel), but the dispersion increases and older ages dominate at larger radii. The IQR goes from 0.4 dex at the first bin to 0.9 dex at the 22.5 arcsec bin. There is also a little increment in the median, from $10^{7.3}$ to $10^{7.8}$yr, consistent with the positive age gradient in Fig. 4. The box plot profile shows that it is almost flat in the inner regions up to the 13.5 arcsec bin, when it ascends up to a maximum at the 16.5 arcsec bin (where the IQR is 0.8 dex). This maximum is therefore responsible for the positive gradient in Fig. 4.

The maximum at the 16.5 arcsec bin is visible in the general profile (dark grey in Fig. 5), in the north-west (red), in the north-east (blue), and in the south-east (orange) quadrants. The south-west (green) quadrant is the only one that does not show this feature in its profile, but the stellar age gradient is clearly positive there too. Remarkably, the youngest age profiles in Fig. 6 (centre) follow a similar trend to the box plot profiles in Fig. 5.

It is not obvious from the RGB images (left panels of Fig. 2) nor from the age maps (right panels of Fig. 2) what is causing the maximum. The ring position, as determined by R. Romano et al. (2008) is located at 20 arcsec, so this maximum does not overlap with the ring. In Fig. 2 we can see what appears to be the bulge close to the east part of the ring, which could explain that this increment in age is the highest for the south-east quadrant (orange in Fig. 6.), but this should have no effect in the western quadrants.

Table 2. $\nabla t_{\star y}$ taken from Fig. 6; for the general gradient and for each quadrant in the anticlockwise sense, where colour description coincides with such figures. All gradient units are in $\log_{10}$(yr).

Galaxy	$R_{\rm ring}$ (kpc)	$\nabla t_{\star y}$ (black)	$\nabla t_{\star y1}$ (red)	$\nabla t_{\star y2}$ (blue)	$\nabla t_{\star y3}$ (orange)	$\nabla t_{\star y4}$ (green)
Arp 143	10.0	-2.2 ± 1.0	-1.6 ± 0.8	-2.6 ± 0.7	-2.0 ± 0.7	-2.5 ± 0.6
NGC 2793	2.3	0.5 ± 0.7	-0.3 ± 0.4	0.4 ± 0.5	1.3 ± 0.6	1.0 ± 0.7
VII Zw 466	11.0	-1.3 ± 0.4	-0.9 ± 0.4	-0.1 ± 0.3	0.1 ± 0.3	-1.4 ± 0.2

We also want to note that in the south-west (green) quadrant (the only one without the maximum) the H α emission is scarcer than in the other quadrants. Considering this, we propose a possible explanation for this stellar age maximum: The whole galaxy formerly had a positive stellar age gradient throughout the outer regions, similar to the south-west quadrant. Afterwards, when the current star formation burst appeared in the outskirts, it caused the median age values to go down in those regions, consequently producing a local descend in the profile. This scenario could effectively explain the maximum observed in the two eastern quadrants and in the north-west quadrant (i.e. where the H α emission is prominent). As for the south-west quadrant – devoid of prominent H α emitting regions – the recent star formation burst probably did not have a significant effect there, preserving the original positive gradient all the way outwards, as observed. Although most low-redshift dwarf galaxies show flat to slightly negative stellar age gradients – both in the inner and outer regions – cases with positive gradients also exist (e.g. see fig. 8 by M. Cano-Díaz et al. 2025).

Regarding the increment in the IQR towards larger radii, it could be explained by the increment in the number of spaxels used in each bin.

Observed star formation characteristics, namely the presence of star formation inside the ring and the positive age gradients, rule out this galaxy as a genuine collisional ring galaxy, in spite of a ring present in the H α image.

4.3.3 *VII Zw 466*

VII Zw 466 is part of a system formed by (apparently) four galaxies and shows an evident ring morphology (Fig. 2, bottom panels). In order to unveil which of the four galaxies was the one that collided with VII Zw 466, we captured the whole system with two fields of the instrument, with part of them overlapping (see the top panel of Fig. 8). The group is catalogued by the Uppsala General Catalogue of Galaxies (P. Nilson 1973) as UGC 07683.

Despite VII Zw 466 showing the smallest angular size of the three galaxies, it presents a larger H α luminosity. Up to 92 per cent of the H α emission originates in the western half of the ring. A small region with redder colours and mass-weighted ages $\leq 10^{10}$ yr is present in the inner border of the west side of the ring, which could be associated with the bulge of the original disc galaxy.

This galaxy has the most complete ring in the sample, with a semi-major axis distance of 9.3 arcsec. With the $S/N > 10$ criterion for the continuum, many spaxels in the inner regions get excluded. Indeed, in J. C. Theys & E. A. Spiegel (1976), VII Zw 466 was classified as a 'RE' galaxy, i.e. elliptical ring with empty interior. VII Zw 466 shows a clear negative age gradient, as expected from a collision scenario.

The interior of the ring appears empty, with only the red quadrant containing a bin at 1.5 arcsec. In its general profile (Fig. 5) VII Zw 466 exhibits a negative gradient. This trend is also observed in the western quadrants (red and green) but not in the eastern ones (blue and orange), where the gradient appears to be flat. The absence of a gradient in the eastern quadrants may result from the limited number of spaxels with S/N$\geq$ 10 available to resolve the profile in that direction, in contrast to the western quadrants. Consequently, these regions are not representative of the ring and

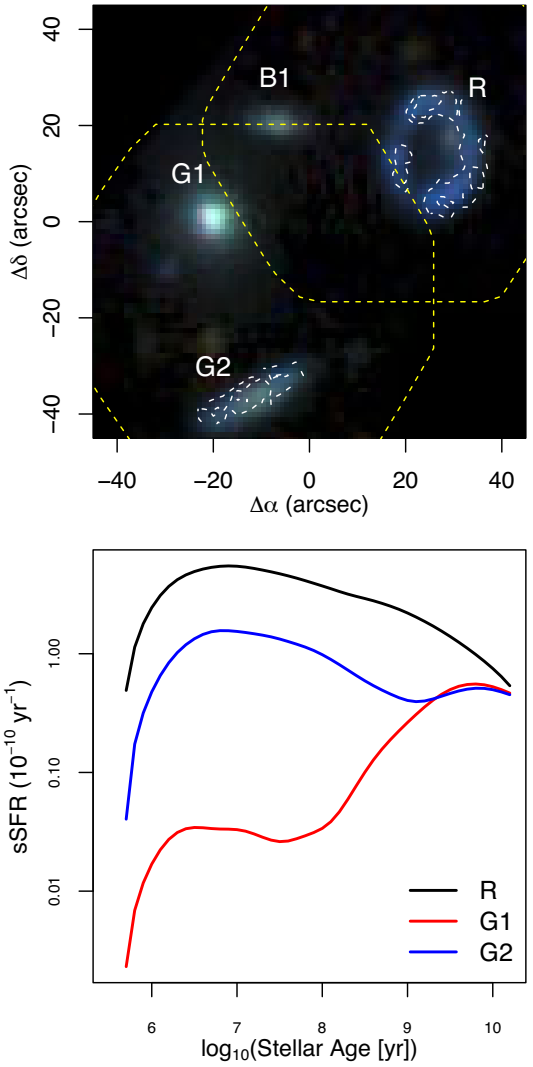

Figure 8. Top: RGB image of the VII Zw 466 group, based on the IFS data, including the two overlapped fields of view (yellow dashed lines). The IDs are consistent with Romano et al. (2008). The NED Identifiers for each galaxy are shown in Table 4. Bottom: sSFH, calculated as the median of the whole spaxels by each galaxy. The horizontal axis shows the stellar age at the moment that the observed light was emitted. Both axes are in logarithmic scale.

would not be suitable for gradient determination. Therefore, we exclude the eastern quadrants from further computations.

VII Zw 466 has a steep youngest-population profile $\nabla t_{\star y}$ (see Table 2). As explained before, and despite all quadrants being taken into account in Fig. 5 (right-panel) and in Table 2, only western quadrants were considered for the general profile. Indeed, the profiles of the eastern quadrants (Fig. 6, blue and orange) appear to be flatter. Due to the projection in the line of sight, we are probably observing only the outer side of the ring of these quadrants, which could explain why we observe younger ages. As a result, the general profile appears to be similar to the western profiles, which are more consistent with that produced after the collision.

The western quadrants (red and green) present more dramatic gradients, with values of $\nabla t_{\star y} \sim -1.0$ and a minimum age of $\sim 10^{7.5}$ yr. The first quadrant (the red one) is hosting what appears to be the original bulge (Fig. 2). This could introduce older populations from the bulge. Despite that, the fourth quadrant (green one), where we do not expect bulge contamination, has even a larger negative value of $\nabla t_{\star y}$.

The youngest populations close to the ring centre in the western half suggest the post-collisional star formation happened around 100–300 Myr ago. In comparison, the star formation in the eastern half stopped as recently as ∼20 Myr ago.

4.4 Profile comparison

Fig. 7 shows a comparison of the general profiles of the three galaxies normalizing the radii by the semi-major axis of their rings (R_{Norm}). The figure shows that Arp 143 and VII Zw 466 profiles have similar steep value of $\nabla t_{\star y}$ of -2.2 and -1.3, respectively, both doubling the error range. It is important to note that the youngest population at low R_{Norm} are old in comparison with the estimated lifetime for the ring from simulations ($\sim 10^7$ yr). For both Arp 143 and VII Zw 466 it is obvious that the youngest stars of the whole galaxy are located in the rings. This is consistent with the collision hypothesis, and, indeed, the internal regions seem to have halted the star formation after the passage of the density wave of the ring.

Meanwhile, the general profile for NGC 2793 (Fig. 6, centre) is almost flat ($\nabla t_{\star y} = 0.5 \pm 0.7$). Compared with the other two galaxies (Fig. 7), this flatness is evident. Such a flat profile is not consistent with the collision hypothesis. Therefore, NGC 2973 is probably not a collisional ring galaxy.

4.5 Expansion velocity of the wave

Obtaining expansion velocities of density waves in ring galaxies is a challenge (E. I. Vorobyov & D. Bizyaev 2003). Previous attempts to measure expansion velocities use gas velocities either from CO or HI lines from the ring (e.g. P. N. Appleton, V. Charmandaris & C. Struck 1996; J. L. Higdon et al. 1997). The spatially resolved ages provide an alternative method to infer the expansion velocity.

The lower limit for the expansion velocity of the wave can be computed by assuming that the age of the youngest population at the impact point (here assumed as the centre of the ellipses, see Section5.1) corresponds to the epoch of the collision and that the wave has been expanding uniformly since then. With an age of the youngest population at the impact point of 300 Myr and ring radius of 10 kpc for Arp 143, and 100 Myr and 11 kpc for VII Zw 466, we estimated expansion velocities of 33 ± 15 and 108 ± 30 km s^{-1}, respectively.

For both galaxies, we find that our measured velocities differ from those reported in the literature. In the case of Arp 143, our value is significantly lower than the expansion velocity of 118 ± 30 km s^{-1} of the CO gas in the ring reported by J. L. Higdon et al. (1997).

In the case of VII Zw 466, our velocity estimation of 108 ± 30 km s^{-1} is about three times higher than the one by P. N. Appleton et al. (1996). They reported an expansion velocity of 32 km s^{-1} for VII Zw 466 using the HI gas in the ring. In this case, the authors did not provide an uncertainty estimation.

Stellar velocities estimated in this work trace the time-averaged velocity of the propagating star formation wave, whereas the velocities of the gas in the ring trace the instantaneous velocity of the expanding density wave. For a uniformly expanding density wave, the two velocities are expected to coincide. The differences suggest non-uniform expansion of the density waves. It should also be considered that the radio beams used for measurement of gas velocities are large, so as to be affected by effects of stellar feedback. Higher spatial resolution observations in both these tracers are required to carry out an elaborate discussion on the nature of the expansion of the density wave.

4.6 The companions of VII Zw 466

As mentioned, VII Zw 466 is part of a group of apparently four galaxies known as UGC 07683 (P. Nilson 1973). While the individual galaxies are registered in the NASA/IPAC Extragalactic Database with proper names, we followed the P. N. Appleton et al. (1996) nomenclature to label the group members G1 and G2, and the background galaxy B1 while we assigned the ID R to VII Zw 466. The NED identifiers, ID and properties of the field galaxies are shown in Table 4.

We observed the whole system using two pointings of the telescope (with their fields of view overlapped) to determine which of the galaxies is the one that collided with VII Zw 466. The complete group of VII Zw 466 is shown in the top panel of Fig. 8. This RGB reconstruction was obtained similarly to the RGB images in Fig. 2.

We determined the optical continuum and emission radial velocities of the system (v_c and v_e, respectively) by integrating the central spaxels (SN $\geq$ 30) of each galaxy in a radius of 3 arcsec. The measurements were obtained using the XCSAO and EMSAO tasks from the RVSAO package (D. J. Mink & M. J. Kurtz 1998) within IRAF (D. Tody 1993). These tasks perform cross-correlation between our spectra and a library of extragalactic objects to account for the continuum. Whenever possible, v_e was directly estimated by fitting the emission lines. The results are presented in Table 4.

The optical velocity we derived for VII Zw 466 is consistent with the HI velocity reported by P. N. Appleton et al. (1996). We also measured optical velocities for galaxies G1 and B1, which lack previously reported HI emission. Our results represent a significant improvement over the approximate optical velocities from J. C. Theys & E. A. Spiegel (1976) for these two galaxies. In agreement with their work, we find that B1 exhibits a significantly different radial velocity compared to the other members of the system. This discrepancy confirms that B1 is a background galaxy rather than a gravitationally bound component of the group.

On the other hand, for the suspected companion G2, our velocity is 14 224 km s^{-1}, which is clearly outside the 14334–14516 km s^{-1} velocity range reported by P. N. Appleton et al. (1996).

Interestingly, G2 reappears in their HI channel map (their fig. 8) in just one channel (14221 km s^{-1}) consistent with our optical velocity. This points to the possibility that the HI structure associated with G2 by P. N. Appleton et al. (1996) was part of the plume connecting G2 with VII Zw 466, and that the real velocity of G2 was the one measured by the Hα line. This would make G2 differ by as much as 350 km s^{-1} in velocity with respect to the ring galaxy, suggesting an impact at a higher velocity than previously thought.

P. N. Appleton et al. (1996) suggested G2 as the most likely intruder. However, they did not rule out the possibility of G1 playing some role. To investigate this possibility, we analyse the specific star formation history (sSFH) of the three group members R, G1, and G2. The sSFH traces the evolution of the specific star formation rate (sSFR; star formation rate per unit stellar mass) of the galaxy over time. Following N. V. Asari et al. (2007), the sSFR is defined as

$$\mathrm{sSFR}(t_\star) = \frac{1}{M^c_\star}\frac{dM^c_\star(t_\star)}{dt_\star} \sim \frac{\log e}{t_\star}\frac{\mu^c_s(t_\star)}{\Delta \log t_\star}, \quad (4)$$

where $t_\star$ is the age of the SSP, sSFR($t_\star$) is the specific star formation rate at $t_\star$, $M^c_\star(t_\star)$ is the mass of gas converted into stars at that age, and $\mu^c_s(t_\star)$ is the fraction of the stellar mass accumulated over the galaxy's history at that age.

Since the three galaxies (R, G1, and G2) are at about the same redshift, they are observed at the same lookback time. This allows us to directly compare their SFH with their stellar ages being consistent among them. In addition, the sSFR was convoluted with a Gaussian filter in $\log t_\star$ with an FWHM of 1 dex, in order to smooth the sSFH curves accounting for the relatively high uncertainties in time of the population synthesis technique.

These curves are shown in the bottom panel of Fig. 8, where the sSFR of the three galaxies is plotted against the stellar age. The plotted sSFHs were taken as the median by bin of the sSFH from all the spaxels of each galaxy. The curve for G1 (red) clearly differs from the other two galaxies. At large stellar ages ($\sim 10^{10}$ yr), the three galaxies had similar sSFR. This is not surprising since they form a group, and they are expected to originate and evolve in a common environment.

At more recent stellar ages their evolutionary paths diverge. The elliptical companion galaxy G1 reaches its peak at early times in its formation history and is dominated by old stellar populations, with little recent star formation. This star formation history is typical of early-type galaxies observed in surveys such as SDSS and CALIFA (i.e. N. V. Asari et al. 2007; R. Cid Fernandes et al. 2013).

On the other hand, both the ring galaxy (black) and the suspected companion G2 (blue) reach their highest peak of sSFR at more recent times ($< 10^9$ yr). The sSFR for the ring galaxy and G2 start deviating strongly from that for G1 at a stellar age of a few hundreds of million years, which is consistent with the collision epoch derived from radial age profiles (Fig. 5).

The plot points to both R and G2 passing through a recent episode of high star formation that did not affect G1. The temporal synchronization of the sSFR curves of these two galaxies reveals compelling evidence for a common recent evolution, likely triggered by the same event: the collision.

5 DISCUSSION

5.1 On the collision geometry

As mentioned in Section 3, we assume a centred collision with the impact point close to the centre of mass, implying that the centre of the ring is also the impact point. Scenarios with the compact galaxy impacting the disc galaxy off-centre were considered in simulations by A. Toomre (1978) and were explored in more detail by P. N. Appleton & C. Struck-Marcell (1987). Their results show that in the case of an off-centre collision, the shock wave is expected to produce a ring with azimuthal asymmetries in the star formation rate, Hα luminosity, etc. As a result, rings could have a radially asymmetrical appearance, where the collision effects will be more important in some directions than in others.

For our sample, the three galaxies show important asymmetries in the Hα emission – and hence in star formation – distribution along the rings, evident from the contours in Fig. 2. In the case of Arp 143 these asymmetries were studied by P. Beirão et al. (2009) using *Spitzer* IR bands and *GALEX* UV bands. They confirm the origin of the star formation knots of the ring as being simultaneously produced by a shock wave detected with H_2 emission. They find their results consistent with the off-centre collision scenario by P. N. Appleton & C. Struck-Marcell (1987), with the formation of the ring resulting from a combination of an expanding wave and a disc rotation movement.

That said, we want to argue in favour of our decision to assume the centred collision scenario to measure the gradients. For Arp 143 the youngest age profiles in Figs 6 and 7 show that the oldest among the youngest spaxels are located closer to the origin, producing the negative age gradient that we report. In the case of VII Zw 466, we see the same trend for the western quadrants (red and green in Fig. 6) with the oldest among the youngest ages being closer to the centre of the ring and a clear negative age gradient, consistent with the centred-collision hypothesis. In the case of the eastern quadrants, the lack of spaxels in the inner regions prevents us from obtaining conclusions. Since we no longer consider NGC 2793 as a collisional ring, we will not discuss its case.

Considering other kinds of asymmetries is also relevant for our sample. A. Toomre (1978) showed that off-centre collisions produce rings with the centre separated from the original bulge of the disc galaxy. The possible original bulge of either of our two collisional ring galaxies is not exactly at the centre of its ring. Therefore it is possible that the intruder galaxy did not impact properly in the ring centre in either of the two cases. In the case of Arp 143, the bulge is slightly de-centred. This points to the possibility that even if the impact was off-centre, it was only slightly so (similar to row 5 in fig. 5 by A. Toomre 1978).

In addition, we are limited by the spatial resolution of our data (∼1.5 arcsec seeing and 1 arcsec spaxel size), comparable with the projected distances from the bulges of the two galaxies to the centres of their rings (a few arcsec); this could effectively blur the effects of this asymmetry on the gradients for the central regions.

In conclusion, given the clear negative gradients of the youngest age profiles and the limitations in spatial resolution of our data, the centred collision scenario is good enough for our purpose. Further studies with higher spatial resolution and better spectral resolution (to determine kinematics) could help to localize the impact point, as suggested by P. N. Appleton & C. Struck-Marcell (1987).

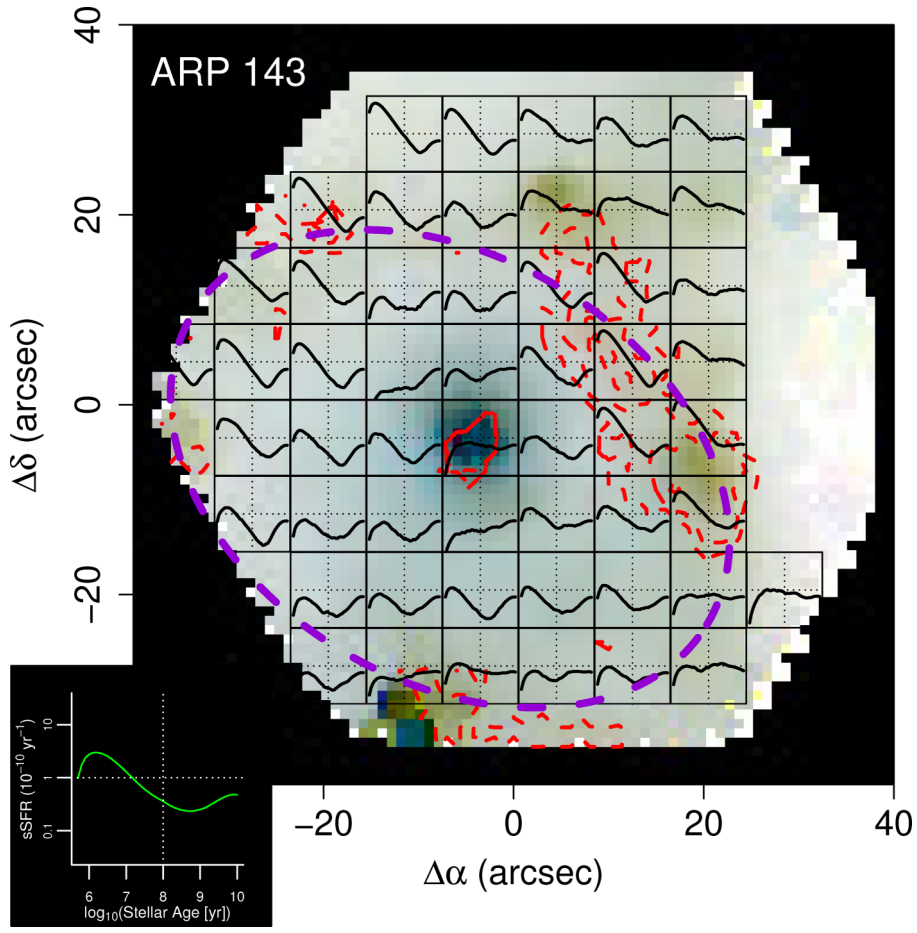

Figure 9. sSFH functions on the RGB negative map of Arp 143. Each box shows the median sSFH function produced by the contributing spaxels, drawing on them. The contributing spaxels correspond to an 8 × 8 array of spaxels, just where the box is located. S/N criterion was relaxed to incorporate all spaxels in the internal region of the ring. The scale of these plots is shown in the bottom-left corner, also showing the median sSFH of all spaxels of the galaxy (in green). H α luminosity contours are shown in red, and the R. Romano et al. (2008) ellipse is shown in violet. sSFH plot axes are in logarithmic scale.

5.2 Spatially resolved specific star formation rates

The IFS data allows us to carry out a spatially resolved analysis of the sSFH (i.e. sSFR versus stellar age, see Section 4.6). Such maps could help us to analyse the – up to one order of magnitude – age differences for the youngest populations between the four quadrants of our classical ring galaxies Arp 143 and VII Zw 466 (see Fig. 6), despite all quadrants presenting similar steep negative gradients in their youngest age profiles. As discussed before, these negative gradients are due to star formation radially propagating outwards over the last $\sim$ 10^8 yr and are expected in ring galaxies.

Both galaxies have $\nabla t_{\star y} < -1.0$ dex. The 'traditional' collision hypothesis would explain these gradients as follows: the passage of the density wave through a region produces a local starburst and the light-weighted ages are dominated by the young massive stars produced in the process. As the wave abandons the region and the starburst stops, the most massive stars die and the light-weighted ages are progressively dominated by a mix of the young low-mass stars generated by the wave and the old low-mass stars formed before the collision. Therefore the ring wave naturally produces an inside-out quenching of star formation in its wake and a light-weighted mean-age gradient is formed between the location of the ring dominated by the youngest ages and the centre (or the impact point) dominated by older ages.

In order to understand the differences in ages of the most recent star formation activity between the four quadrants, we mapped the sSFH of each of our sample galaxies. We consider the sSFR as a proxy for the SFR, and use these maps to understand the morphology of post-collision star formation. We divided each image into an array of sectors formed by 8×8 spaxels for Arp 143 and NGC 2793 to increase the S/N ratio. For VII Zw 466, we used a smaller array of 5×5 due to the smaller angular size of that galaxy. The grouping compensates for the lower S/N spaxels, allowing for a more robust coverage of the disc. The resulting median sSFH for each sector is plotted in boxes on (inverted colour) RGB maps (Figs 9, 10, and 11 for Arp 143, NGC2793, and VII Zw 466, respectively). The median sSFH for each galaxy is included as an inset for reference. The positions of the dotted vertical and horizontal lines are the same in all subplots as in the insets.

As the density wave created by the collision expands, it is expected to locally increase the sSFR in the sectors of the disc at which it arrives. The median sSFH of the whole galaxy for Arp 143 (bottom-left inset in Fig. 9) best illustrates the effect of expanding wave. It shows two main peaks of high star formation. The peak corresponding to older ages ($> 10^9$ yr) repre-

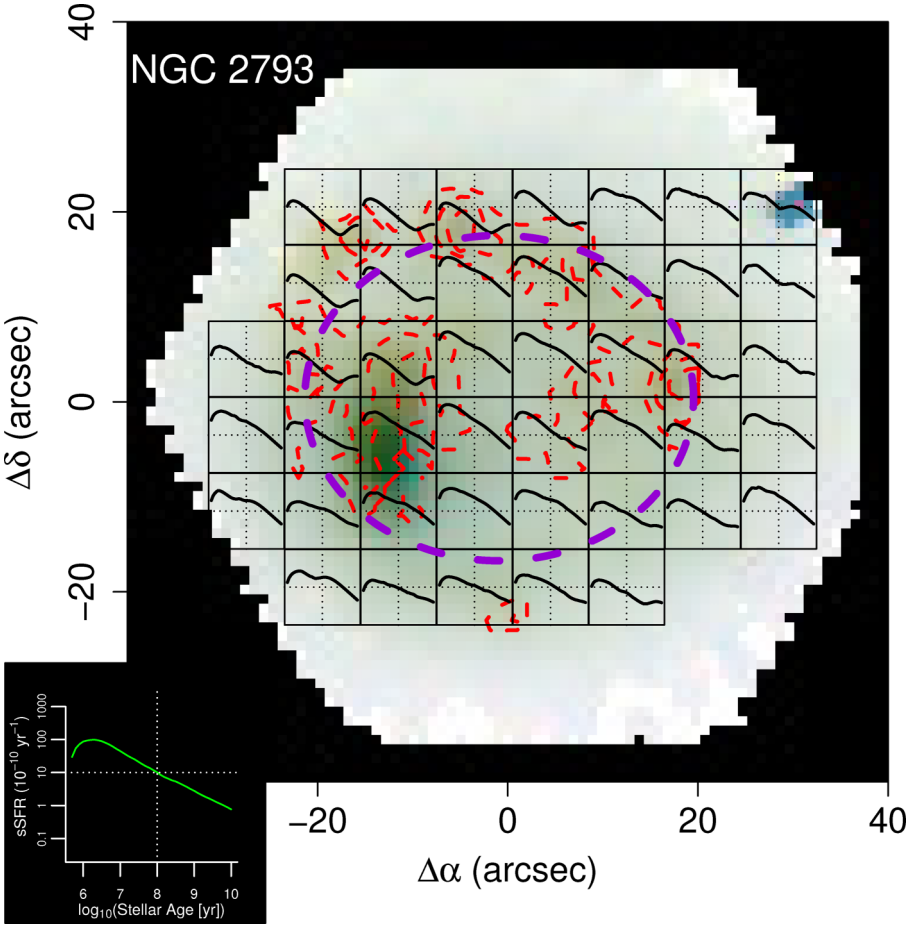

Figure 10. Same as Fig. 9 for NGC 2793. It is important to figure out that the scale is different.

sents clearly the stellar populations of the pre-collision (bulge-dominated) galaxy, with the high sSFR at the beginning of galaxy formation followed by a decrease. However, except for very well-bound regions like the bulge, this 'first' peak is generally not representative of the regions where these stars now reside. This is because stars formed in such early star-forming episodes are unlikely to remain in their original regions due to the disc rotation or other kinds of migration (e.g. the one induced by the collision). We refer to the first peak as the 'pre-collisional peak' and the more recent maximum as the 'post-collisional peak'. The monotonic decrease is halted at around $\log_{10}(\text{Age}\,[\text{yr}]) = 8.5$, the estimated epoch of the ring-making collision. The sSFR smoothly increases thereafter.

The sSFH in most of the sectors at the position of the ring – especially at the Hα-emitting regions (red contours) – follows the global trend (the median sSFH of the galaxy is shown in the inset in the figure), with the peak at the current epochs ($\log_{10}(\text{Age}\,[\text{yr}]) < 7.0$) being stronger than the sSFR corresponding to populations of the pre-collisional peak ($\log_{10}(\text{Stellar Age}\,[\text{yr}]) > 9.5$).

The age when the minimum in the sSFH occurs varies only slightly in the zones with and without Hα. This suggests that even the zones in the ring, far from the impact point, contain stellar populations formed just after the collision. In the classical density wave models of J. C. Theys & E. A. Spiegel (1976), this would not be possible, since the stellar populations formed during the passage of the wave are left behind at their formation sites. On the other hand, the stellar populations are dragged by the wave in the recent simulations by F. Renaud et al. (2018), allowing us to find the first stellar populations formed by the impact as far out as the ring position. This scenario is consistent with our observations.

The sSFH show a distinct shape in the southern part of Arp 143, suggesting an asymmetric expansion of the ring. Some enhancement in the sSFR over the last $\sim 10^8$ yr is seen, but only mildly in comparison with the northern regions. It is worth noting that the northern regions are currently closer to the companion galaxy than the southern regions. The boxes belonging to the bulge and the surrounding zones also show minimum enhancements following the collision.

Fig. 9 also plots some boxes to the north and outside of the ring. There is a tidal bridge of stars connecting both galaxies, also visible in Fig. 2. Their sSFHs and the young values of the mean light-weighted ages are consistent with the presence of young massive stars formed as a consequence of the impact. A detailed kinematics study of this region, in synergy with the results presented here, could reveal if these stars were formed in situ inside this bridge from gas dragged from the disc by tidal forces, or if they were formed first in the disc – most possibly in the ring – and were tidally dragged out afterwards.

From the earlier discussion, NGC 2793 does not appear to follow the collision scenario, both for the ring and the inner re-

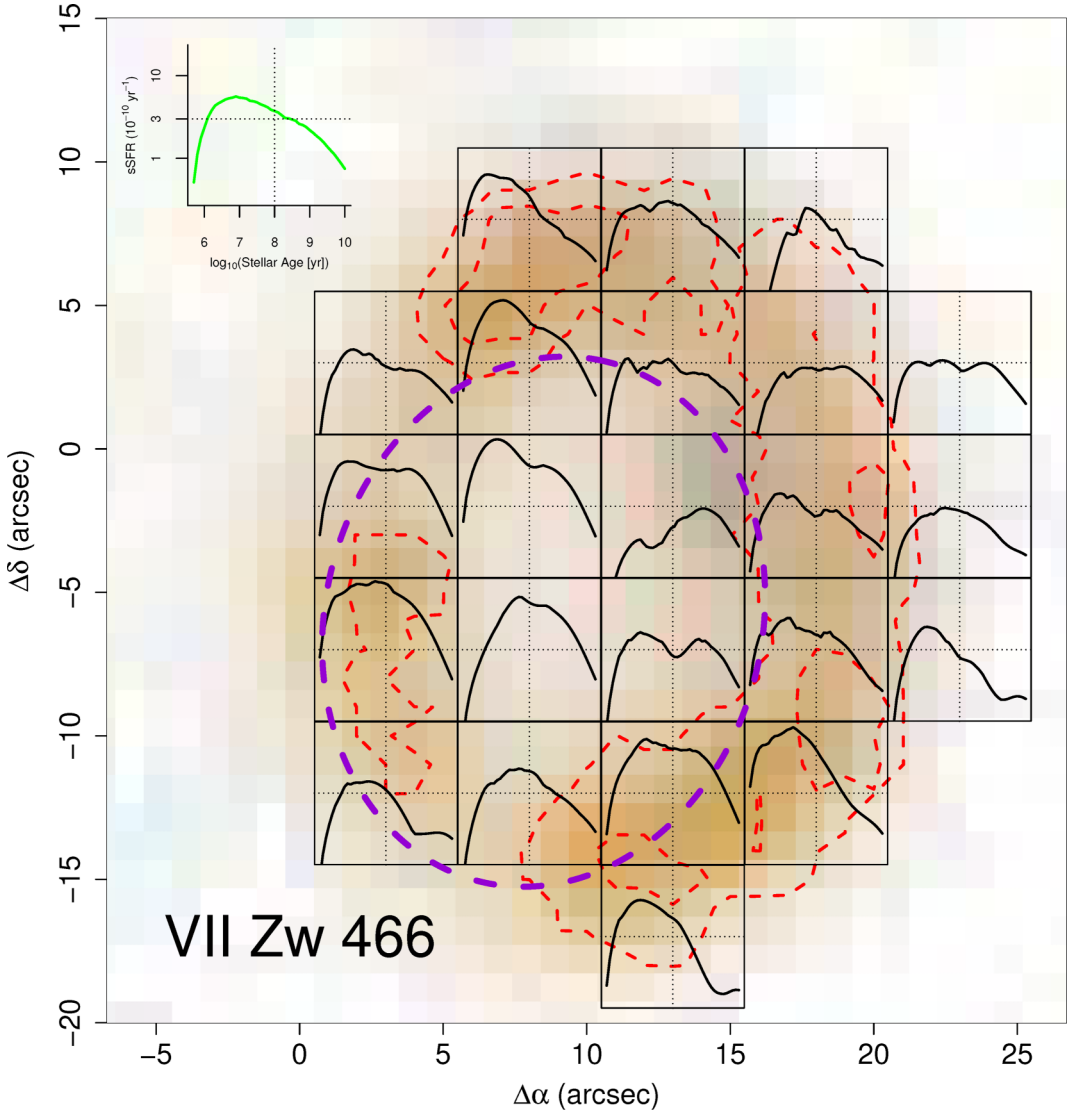

Figure 11. Same as Fig. 9 for VII Zw 466. Now the number of contributing spaxels was reduced to a 5×5 array to compensate for the smaller angular size of this galaxy.

gions. Indeed, according to Fig. 10, it suffered recent intense star formation across the whole galaxy, with the oldest peak of sSFH not distinguishable in most boxes. This is consistent with the flat youngest age profile shown in Fig. 7 in comparison to the other two galaxies (and the almost zero $\nabla t_{\star,y}$ in Table 2). Therefore, this evidence appears to confirm that NGC 2793 is not a collisional ring galaxy.

For the empty-ring galaxy VII Zw 466, the two peaks in the sSFR are not easily discernible (Fig. 11). The first peak – corresponding to the formation of the pre-collision stellar populations – can be noticed only in a few boxes to the south and south-west outside the ring. Many of the rest of the boxes show abrupt enhancement of sSFR at $\sim 10^8$ yr, the estimated collision epoch. Remarkably, this enhancement in the star-forming activity is not just restricted to the ring regions, but is also present in the empty inner regions. The time at which the enhancement occurred does not have a clear radial dependence, suggesting that the ring contains stellar populations dragged by the wave, similar to the behaviour found in Arp 143.

5.3 Current location of the density wave

The decomposition of light in stellar populations of distinct ages at each spaxel allows us to construct the radial profile of intensities from stars formed before the collision and after the collision. To do that, we separated the flux contribution of populations with pre-collision ages from those with post-collision ages in each spaxel. The flux (dust-corrected) was integrated in the range of 3800–7200 Å, i.e. the same range used for the stellar population synthesis. We then produced radial profiles that are shown in Fig. 12, keeping NGC 2793 for the sake of completeness.

According to simulations (F. Renaud et al. 2018), the expanding density wave not only triggers new star formation in the ring but may also transport pre-existing disc stars. Consequently, the light distribution of these pre-collisional stars might also roughly trace the density wave. Indeed, Fig. 12 shows that while the post-collisional young populations (black solid line) dominate the optical emission at the ring radius (grey dashed line), the old pre-collisional populations (red solid line) also exhibit enhanced flux at that radius.

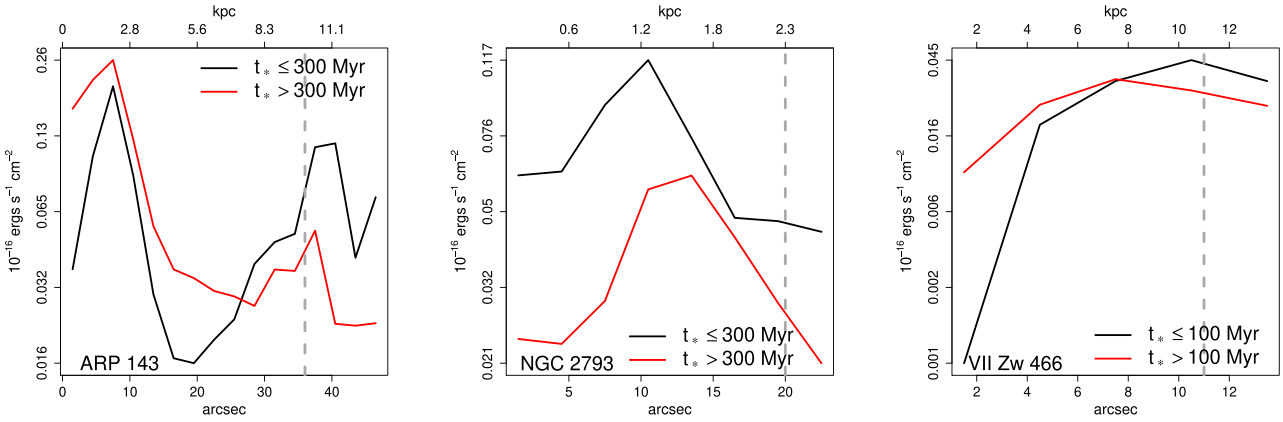

Figure 12. Comparison of the intensity profiles derived from the integrated flux of population with pre-collisional (red) and post-collisional (black) ages in the three galaxies. The current position of the ring is shown by the dotted vertical line. See the description of results for each galaxy in the text for details.

For Arp 143 (left panel in Fig. 12) the peak at radius < 10 arcsec corresponds to light from the bulge, with contribution from both pre-collisional and post-collisional stellar populations, with the flux dominated by the former. The peak in the black line beyond the central bulge is consistent with the position of the ring and illustrates the current position of expanding density wave dragging pre-collisional stars. The figure shows that this second flux peak of pre-collisional stars is consistent with a flux peak of post-collisional stars formed by the passage of the wave. This spatial coincidence indicates that the density wave (as traced by pre-collisional stars) is effectively the most suitable cause for the presence of a star formation in the ring (as traced by post-collisional stars and H α emission). The fact that the young population's profile enhancement extends well beyond the ring radius while the older populations' peak decays faster after that radius can be explained by the presence of the tidal bridge in the north-western part of the ring dominated by young light-weighted ages.

For VII Zw 466, we can see a similar pattern as with Arp 143, with the pre-collisional stars profile growing towards the ring along with the post-collisional profile, although with notable differences. First, since this galaxy is an 'empty' ring, with the possible bulge located in the inward part of the ring (therefore not close to the ring centre), the low-radius peak is not present. Second, there is a clear misalignment of both peaks, with the post-collisional profile peaking at the ring position and the pre-collisional profile peaking $\sim$ 3 arcsec inward. This is explained by the presence of the bulge, strongly dominated by pre-collisional stars (like in Arp 143). Beyond this point the flux in the ring is clearly dominated by post-collisional stars (also like in Arp 143). Notice also that due to the small angular size of VII Zw 466, spatial resolution is poorer for this galaxy and the shape of the profiles is not clearly defined. Yet the effects described above are clearly discernible.

Fig. 12 shows that the density wave is, as expected, currently at the position of the star-forming ring in both galaxies. IFS data allowed us, for the first time, to isolate the light of pre-collisional stars from that of the post-collisional stars thus addressing the long-standing question on the current location of the density wave (see e.g. A. P. Marston & P. N. Appleton 1995; R. A. Gerber et al. 1996). The results are in agreement with F. R. Ditrani et al. (2024), which found that most of the spectral luminosity at the ring location is dominated by such post-collisional stars for the Carthwheel galaxy.

Our data show a density wave in the old stars, illustrating the response of these pre-collisional stars to the ring-making collision. The limited spatial resolution and the presence of tidal features in our data prevent us from examining whether the density wave is effectively ahead of the star-forming wave as expected in classical models (e.g. R. A. Gerber et al. 1996). Future IFS observations of these classic ring galaxies at higher spatial resolution will be invaluable in addressing this question.

6 SUMMARY AND CONCLUSIONS

We tested the collision hypothesis of ring galaxies through a stellar population analysis with IFS data of three ring galaxy candidates. The galaxies come from the R. Romano et al. (2008) sample and they were observed with the Calar Alto 3.5 m telescope, using the PMAS/PPaK spectrophotometer.

For each galaxy we produced an RGB map, the Mean Age maps weighted by light and by mass (Fig. 2), we found that light-weighted mean age is the most appropriate to characterize the young populations created by the impact and hence the ring.

The collision hypothesis predicts the presence of a negative radial age gradient generated by the moving front of star formation triggered, which in itself is generated by the passage of the density wave. We looked for this gradient by plotting radial profiles of light-weighted mean ages. We also plotted radial profiles for the different quadrants of each galaxy to account for possible azimuthal asymmetries (Fig. 5).

Then we produced another set of radial profiles that better represent the last major episode of star formation at each radius by statistically selecting the youngest spaxels (in terms of light-weighted mean age) at each radius (Fig. 6). This allowed us to compute the youngest ages gradient ($\nabla t_{\star y}$) as a function its distance from the ring centre. With these gradients we estimated the lower limits for the age of the collision and for the radial velocity of the wave. These calculated quantities are presented in Table 3. An sSFH analysis was also performed using equation (4).

We found that the Arp 143 and VII Zw 466 galaxies show negative age gradients consistent with the collision hypothesis, with the youngest population ageing smoothly as we move from the ring position inwards. We estimated a lower limit for the

Table 3. Parameters derived from the analyses performed in this study.

Galaxy	$\nabla t_{\star y}$	Collision age	Expansion velocity	
	$\log_{10}$(yr)	(Myr) ago	(km s^{-1})	(kpc Gyr^{-1})
Arp 143	-2.2 ± 1.0	300	33 ± 10	33 ± 10
NGC 2793	$\sim 0.0 \pm 0.5$	-	-	-
VII Zw 466	-1.3 ± 0.4	100	108 ± 28	110 ± 29

collision age of 300 and 100 Myr for Arp 143 and VII Zw 466, respectively, assuming that the youngest ages at the ring centres correspond with the collision age. Assuming a uniform propagation, this corresponds to average expansion velocities of 33 ± 10 and 108 ± 28 km s^{-1}, respectively, for Arp 143 and VII Zw 466 (Table 3).

An analysis of the population properties in the four quadrants suggests noticeable azimuthal variations in the ring which could point to off-centre geometries for the collision. We created spatially resolved sSFH maps by dividing the galaxies into boxes containing a given number of spaxels to increase the SNR. These maps show considerable azimuthal variations with some regions not showing any enhancements in star formation corresponding to the propagation of the wave. In zones where enhancements in sSFRs are noticeable, the regions in the ring as well as those near the impact point, show enhancements at the same time. This suggests that the stellar populations formed during the propagation of the wave could have been dragged by the wave to its current position in the star-forming ring, as predicted in the recent models for Cartwheel-like rings by F. Renaud et al. (2018).

We also measured the redshifts of the four members of the VII Zw 466 group, confirming that one of them (B1) is really a background galaxy. We used the sSFH of the other three galaxies, which showed that G2 has recent star formation activity consistent with the one in the ring, which is not the case with the other group member, G1. Therefore, G2 was most likely the galaxy that impacted with VII Zw 466 causing the formation of the ring. This is consistent with the HI bridge connecting both galaxies reported by P. N. Appleton et al. (1996), and confirming their results.

In comparison, the behaviour of the stellar population ages in NGC 2793 is different from the other two galaxies. We notice that this is a low-mass galaxy and one of the smallest rings of the R. Romano et al. (2008) sample, with only ~ 2 kpc radius. Star formation is expected to be quenched as the wave moves outwards due to negative feedback effects of supernova explosions and gas consumption over a time-scale of a few tens of million years. The recent star formation is very similar in all the regions of the galaxy, both in the ring and in the inner regions. In addition, the age of the supposed ring is about 10^7 yr old Table 3), but its value is in the range of the young populations across the whole galaxy and not only in the ring. All the evidence supports that NGC 2793 is not a true collisional ring galaxy.

In this work, we showed that the combination of IFS and stellar population synthesis is an invaluable tool for observationally testing the predictions of different theoretical collisional scenarios. The application of these techniques to larger samples of collisional ring galaxy candidates combined with higher spatial and spectral resolution instruments will help to disentangle the details and history of such extreme collisions and the transformation suffered by galaxies that pass through this process.

ACKNOWLEDGEMENTS

This paper is proudly, to our knowledge, the first ever peer-reviewed paper in astrophysics led by astronomers working from Nicaragua. MC-M and AR-O dedicate this work to José H. Peña (Instituto de Astronomía, UNAM, Mexico), whose long-standing efforts to promote professional astronomy among young researchers in Central and South America made this achievement possible.

We thank the referee for the insightful comments that helped to improve the quality of this paper.

RG-B acknowledges financial support from the Severo Ochoa grant CEX2021-001131-S funded by MCIN/AEI/10.13039/501100011033 and the grant PID2022-141755NB-100.

DATA AVAILABILITY

The observational data are publicly available through the Calar Alto Observatory archive (https://www.caha.es/access-and-services/public-archives) under program F17-3.5-027 with PI R. Ortega-Minakata. Programming code used for this analysis will be made available on reasonable request to the corresponding author.

REFERENCES

Amram P., Mendes de Oliveira C., Boulesteix J., Balkowski C., 1998, A&A, 330, 881
Anderson E. et al., 1999, LAPACK Users' Guide, 3rd edn., Society for Industrial and Applied Mathematics . 3600 University City Science CenterPhiladelphia, PA 19104-2688
Appleton P. N., Struck-Marcell C., 1987, ApJ, 312, 566
Appleton P. N., Charmandaris V., Struck C., 1996, ApJ, 468, 532
Asari N. V., Cid Fernandes R., Stasińska G., Torres-Papaqui J. P., Mateus A., Sodré L., Schoenell W., Gomes J. M., 2007, MNRAS, 381, 263
Athanassoula E., Bosma A., 1985, ARA&A, 23, 147
Beirão P., Appleton P. N., Brandl B. R., Seibert M., Jarrett T., Houck J. R., 2009, ApJ, 693, 1650

Table 4. Galaxies in the group of VII Zw466. ID is the same as in Fig. 8 for consistency with R. Romano et al. (2008), as explained in the text. The radial velocities v_c and v_e are the continuum and emission lines (when possible) radial velocities, respectively, extracted from the integration of the central spaxels inside a radius of 3 arcsec. The estimation of v_c and v_e was obtained using the XCSAO and EMSAO task of RVSAO package (D. J. Mink & M. J. Kurtz 1998) from IRAF software (D. Tody 1993). Mean Age is the median age for all spaxels with SN≥10 in the continuum in each galaxy.

Galaxy NED identifier	ID	RA	Dec.	Mean age log(yr)	v_c (km s^{-1})	v_e (km s^{-1})
VII Zw 466	R	$12^h32^m04.4^s$	$+66°24'16''$	8.15 ± 0.12	14573 ± 14	14530 ± 10
UGC 07683 NOTES02 NED02	G1	$12^h32^m13.2^s$	$+66°23'59''$	9.77 ± 10	13958 ± 12	–
UGC 07683 NOTES02 NED03	G2	$12^h32^m11.7^s$	$+66°23'22''$	8.81 ± 14	14224 ± 2	14225 ± 24
UGC 07683 NOTES02 NED01	B1	$12^h32^m10.8^s$	$+66°24'19''$	9.00 ± 0.30	25008 ± 10	24993 ± 151

Bertelli G., Bressan A., Chiosi C., Fagotto F., Nasi E., 1994, A&AS, 106, 275
Brocklehurst M., 1971, MNRAS, 153, 471
Bruzual G., Charlot S., 2003, MNRAS, 344, 1000
Bundy K. et al., 2015, ApJ, 798, 7
Burbidge E. M., Burbidge G. R., 1959, ApJ, 130, 12
Cano-Díaz M. et al., 2025, AJ, 170, 27
Cardelli J. A., Clayton G. C., Mathis J. S., 1989, ApJ, 345, 245
Carnall A. C., 2017, preprint (arXiv:1705.05165)
Catalán-Torrecilla C. et al., 2015, A&A, 584, A87
Catalán-Torrecilla C. et al., 2017, ApJ, 848, 87
Chabrier G., 2003, PASP, 115, 763
Cid Fernandes R., Gu Q., Melnick J., Terlevich E., Terlevich R., Kunth D., Rodrigues Lacerda R., Joguet B., 2004, MNRAS, 355, 273
Cid Fernandes R., Mateus A., Sodré L., Stasińska G., Gomes J. M., 2005, MNRAS, 358, 363
Cid Fernandes R. et al., 2013, A&A, 557, A86
Cid Fernandes R. C., Leão J. R. S., Lacerda R. R., 2003, MNRAS, 340, 29
Conroy C., 2013, ARA&A, 51, 393
Corwin Harold G. J., Buta R. J., de Vaucouleurs G., 1994, AJ, 108, 2128
de Zeeuw P. T. et al., 2002, MNRAS, 329, 513
Ditrani F. R., Longhetti M., Fossati M., Wolter A., 2024, A&A, 688, A89
Ellison S. L., Sánchez S. F., Ibarra-Medel H., Antonio B., Mendel J. T., Barrera-Ballesteros J., 2018, MNRAS, 474, 2039
Falcón-Barroso J., Sánchez-Blázquez P., Vazdekis A., Ricciardelli E., Cardiel N., Cenarro A. J., Gorgas J., Peletier R. F., 2011, A&A, 532, A95
Galbany L. et al., 2018, ApJ, 855, 107
García-Benito R. et al., 2015, A&A, 576, A135
Gerber R. A., Lamb S. A., Balsara D. S., 1996, MNRAS, 278, 345
Hernquist L., Weil M. L., 1993, MNRAS, 261, 804
Higdon J. L., Lord S. D., Cecil G., 1996, in American Astronomical Society Meeting Abstracts. p. 89.05
Higdon J. L., Rand R. J., Lord S. D., 1997, ApJ, 489, L133
Husemann B. et al., 2013, A&A, 549, A87
Ibarra-Medel H. J. et al., 2016, MNRAS, 463, 2799
Korchagin V., Mayya Y. D., Vorobyov E., 2001, ApJ, 554, 281
Levenberg K., 1944, Quart. Appl. Math., 2, 164
López-Cruz O. et al., 2019, ApJ, 886, L2
Lynds R., Toomre A., 1976, ApJ, 209, 382
Mapelli M., Moore B., Ripamonti E., Mayer L., Colpi M., Giordano L., 2008, MNRAS, 383, 1223
Maraston C. et al., 2020, MNRAS, 496, 2962
Marcum P. M., Appleton P. N., Higdon J. L., 1992, ApJ, 399, 57
Marquardt D. W., 1963, J. Soc. Ind. Appl. Math., 11, 431
Marston A. P., Appleton P. N., 1995, AJ, 109, 1002
Mateus A., Sodré L., Cid Fernandes R., Stasińska G., Schoenell W., Gomes J. M., 2006, MNRAS, 370, 721
Mayya Y. D., Barway S., Gómez-González V. M. A., Zaragoza-Cardiel J., 2024, MNRAS, 527, 2816
Mink D. J., Kurtz M. J., 1998, in Albrecht R., Hook R. N., Bushouse H. A., eds, ASP Conf. Ser. Vol. 145, Astronomical Data Analysis Software and Systems VII. Astron. Soc. Pac., San Francisco, p. 93
Morales-Vargas A. et al., 2020, MNRAS, 499, 4370
Nilson P., 1973, Uppsala general catalogue of galaxies. Uppsala: Astronomiska Observatorium, Uppsala, Sweden
Renaud F. et al., 2018, MNRAS, 473, 585
Romano R., Mayya Y. D., Vorobyov E. I., 2008, AJ, 136, 1259
Sánchez-Blázquez P. et al., 2006, MNRAS, 371, 703
Sánchez S. F. et al., 2012, A&A, 546, A2
Sánchez S. F. et al., 2016, A&A, 594, A36
Schlegel D. J., Finkbeiner D. P., Davis M., 1998, ApJ, 500, 525
Springob C. M., Haynes M. P., Giovanelli R., Kent B. R., 2005, ApJS, 160, 149
Struck-Marcell C., Higdon J. L., 1993, ApJ, 411, 108
Theys J. C., Spiegel E. A., 1976, ApJ, 208, 650
Theys J. C., Spiegel E. A., 1977, ApJ, 212, 616
Tody D., 1993, in Hanisch R. J., Brissenden R. J. V., Barnes J., eds, ASP Conf. Ser. Vol. 52, Astronomical Data Analysis Software and Systems II. Astron. Soc. Pac., San Francisco, p. 173
Toomre A., 1978, in Longair M. S., Einasto J., eds, Proc. IAU Symp. 79, Large Scale Structures in the Universe. Kluwer, Dordrecht, p. 109
Vazdekis A., Sánchez-Blázquez P., Falcón-Barroso J., Cenarro A. J., Beasley M. A., Cardiel N., Gorgas J., Peletier R. F., 2010, MNRAS, 404, 1639
Vazdekis A., Koleva M., Ricciardelli E., Röck B., Falcón-Barroso J., 2016, MNRAS, 463, 3409
Vorobyov E. I., Bizyaev D., 2001, A&A, 377, 835
Vorobyov E. I., Bizyaev D., 2003, A&A, 400, 81
Zaragoza-Cardiel J., Gómez-González V. M. A., Mayya D., Ramos-Larios G., 2022, MNRAS, 514, 1689

This paper has been typeset from a TEX/LATEX file prepared by the author.